Northward Propagation, Initiation, and Termination of Boreal Summer Intraseasonal Oscillations in a Zonally Symmetric Model

Yang, Q., Khouider, B., Majda, A. J., & De La Chevrotière, M.

2019

This article was originally published at:
https://doi.org/10.1175/JAS-D-18-0178.1

Citation for this paper:

Yang, Q., Khouider, B., Majda, A. J., & De La Chevrotière, M. (2019). Northward Propagation, Initiation, and Termination of Boreal Summer Intraseasonal Oscillations in a Zonally Symmetric Model. *Journal of the Atmospheric Sciences*, 76(2), 639-688. https://doi.org/10.1175/JAS-D-18-0178.1

Northward Propagation, Initiation, and Termination of Boreal Summer Intraseasonal Oscillations in a Zonally Symmetric Model

QIU YANG

Center for Prototype Climate Modeling, New York University Abu Dhabi, Saadiyat Island,
Abu Dhabi, United Arab Emirates

BOUALEM KHOUIDER

Department of Mathematics and Statistics, University of Victoria, Victoria, British Columbia, Canada

ANDREW J. MAJDA

Department of Mathematics and Center for Atmosphere Ocean Science, Courant Institute of Mathematical
Sciences, New York University, New York, New York, and Center for Prototype Climate Modeling,
New York University Abu Dhabi, Saadiyat Island, Abu Dhabi, United Arab Emirates

MICHÈLE DE LA CHEVROTIÈRE

Meteorological Research Division, Environment and Climate Change Canada, Montreal, Quebec, Canada

(Manuscript received 22 June 2018, in final form 22 November 2018)

ABSTRACT

A simple multilayer zonally symmetric model, using a multicloud convective parameterization and coupled to a dynamical bulk atmospheric boundary layer, is used here to simulate boreal summer intraseasonal oscillations (BSISO) in the summer monsoon trough and elucidate the underlying main physical mechanisms responsible for their initiation, propagation, and termination. Northward-moving precipitating events initiated near the equator propagate northward at roughly $1^\circ\,\mathrm{day}^{-1}$ and terminate near 20°N. Unlike earlier findings, the northward propagation of precipitation anomalies in this model is due to the propagation of positive moisture anomalies in the northward direction, resulting from an asymmetry in the meridional velocity induced by the beta effect. From a moisture-budget perspective, advection constitutes a biased intrusion of dry air into the convection center, forcing new convection events to form north of the wave disturbance, while moisture convergence supplies the precipitation sink. The BSISO events are initiated near the equator when the competing effects between first-baroclinic divergence and second-baroclinic convergence, induced by the descending branch of the Hadley cell and in situ congestus heating, respectively, become favorable to convective intensification. The termination often near 20°N and halfway stalling of these precipitating events occur when the asymmetry in the first-baroclinic meridional winds weakens and when the negative moisture gradient to the north of the convection center becomes too strong as the anomaly exits the imposed warm pool domain.

1. Introduction

The intraseasonal variability of the tropical troposphere is dominated by wave-like systems with planetary-scale flow patterns strongly coupled with convection and heavy rainfall known by the generic name of intraseasonal oscillations (ISOs; Lau and Waliser 2011). The Madden–Julian Oscillation (MJO; Madden and Julian 1971, 1972), once called the holy grail of tropical atmospheric dynamics (Raymond 2001), has received tremendous attention since its discovery (e.g., Madden 1986; Hendon and Liebmann 1994; Hendon and Salby 1994; Raymond 2001; Biello and Majda 2005; Zhang 2005; Majda and Stechmann 2009; Ajayamohan et al. 2013; Jiang et al. 2015; Zhang 2013). The MJO is a

---

Denotes content that is immediately available upon publication as open access.

Corresponding author: Boualem Khouider, khouider@uvic.ca

DOI: 10.1175/JAS-D-18-0178.1

planetary-scale convective envelope with an intraseasonal period of 40–60 days, occurring over the Indian Ocean–western Pacific warm pool and propagating eastward along the equator at $5\,\mathrm{m\,s^{-1}}$, which typically prevails during the Northern Hemisphere winter season (Zhang 2005). As a counterpart to the MJO, the Indian monsoon boreal summer intraseasonal oscillation (BSISO) is generally associated with the boreal summer MJO and shares many characteristics, such as zonal propagation, period, and moisture dynamics, with the MJO. It typically initiates over the equatorial Indian Ocean, propagates northward at $1^{\circ}\,\mathrm{day}^{-1}$ (about $1.29\,\mathrm{m\,s^{-1}}$), and terminates around 20°N over the Indian subcontinent during boreal summer (Lau and Waliser 2011). The early investigation of the northward propagation of tropical convection dates back to the 1970s, when Yasunari (1979, 1980) identified a northward movement of cloudiness in 30–40-day periods over the Indian Ocean area during the summer monsoon. It is generally believed that the life cycle of BSISO is intimately connected with the Indian monsoon and the Asian summer monsoon (Lee et al. 2013). According to Fig. 2.2 in Lau and Waliser (2011), BSISO is essentially an intraseasonal anomaly of rainfall of comparable magnitude as the monsoonal background circulation.

Much progress in improving the BSISO simulations has been made, but it is far from being satisfactory. The underlying mechanisms associated with the initiation, propagation, and termination processes of BSISO are still poorly understood. A comprehensive elucidation of these physical processes is not only a theoretical curiosity, but it would hopefully provide modelers and weather-prediction scientists with new metrics on how to improve climate and weather forecasting models. Since the BSISO is an important component of intraseasonal variability, the realistic simulation of BSISO should be not only a benchmark for examining skills and behaviors of present-day global climate models (GCMs) but also a potential prediction source for extending the current 2-week subseasonal-to-seasonal prediction skill (Brunet et al. 2010). With the recent developments in computing techniques, resources, and satellite measurements, many efforts have been made to better simulate BSISO in cloud-resolving models (CRMs) and GCMs in terms of its initiation, propagation, and termination processes. Jiang et al. (2004), for example, looked at the spatial and temporal structures of the northward-propagating BSISO based on the analysis of both the ECHAM4 model simulation and NCEP–NCAR reanalysis. Fu and Wang (2004) conducted a series of small-perturbation experiments, and they demonstrated that an atmosphere–ocean coupled model and an atmosphere-only model produce significantly different intensities of BSISO and have shown evidence of strong relationships between convection and underlying sea surface temperature (SST) variations. Seo et al. (2007) have examined the effect of air–sea coupling and the basic-state SST associated with the BSISO by using the NCEP coupled Climate Forecast System (CFS) model.

Many mechanisms have been proposed to explain the northward propagation of the BSISO in the past decades. Based on numerical experiments with a linear primitive equation model with a climatological basic state for July obtained from reanalysis data, Wang and Xie (1997) suggested that the monsoon mean flows and spatial variation of moist static energy trap equatorial disturbances in the Northern Hemisphere (NH) summer monsoon domain, while the mean Hadley circulation plays a critical role in the reinitiation of equatorial Kelvin–Rossby wave packets over the equatorial Indian Ocean. Based on both GCM simulation and NCEP–NCAR reanalysis data, Jiang et al. (2004) propose two mechanisms because of internal atmospheric dynamics for the northward propagation of the BSISO, namely, the generation of the northward-displaced barotropic vorticity and the moisture–convection feedback. The first mechanism is further examined in a zonally symmetric model setup (Drbohlav and Wang 2005) and a three-dimensional intermediate model (Drbohlav and Wang 2007). By using lagged regressions of intraseasonally filtered outgoing longwave radiation (OLR), Lawrence and Webster (2002) suggested a link between the eastward and northward movement of convection, which is believed to be consistent with an interpretation of the BSISO in terms of propagating equatorial modes. Besides, Rossby waves emitted by equatorial convection and air–sea interactions are found to play a critical role in the BSISO dynamics (Kemball-Cook and Wang 2001).

Among most of the theoretical and numerical studies based on intermediate models, the warm surface temperature near the equatorial regions received much less attention than that over the Indian monsoon regions. As pointed out by Sikka and Gadgil (1980), there exists a seesaw characteristic of maximum cloud zones over the Indian longitudes of 70°–90°E; one of which is near the equator and the other of which is along 15°N, consistent with the simulations of Ajayamohan et al. (2014).

Meanwhile, in the aforementioned models (Wang and Xie 1997; Drbohlav and Wang 2005, 2007), the nonlinear advection terms in momentum and thermal equations are replaced by mean-flow advection by assuming that the BSISO is a relatively small perturbation. Such simplified models ignore the possible internal mechanisms involving nonlinear advection effects, which may be revealed to be important, given that the BSISO disturbances are comparable to the background mean monsoon circulation (Lau and Waliser 2011). Our motivation here stems from these limitations and the success of a recently developed multicloud parameterization technique, mimicking the main cloud types observed in the tropics and their interactions with the environment, in reproducing the key observational features of the tropical modes of variability associated with organized convection, including northward-propagating BSISOs, in both simple models (Khouider and Majda 2006b, 2008b,a; Waite and Khouider 2009) and GCMs (Khouider et al. 2011; Ajayamohan et al. 2013, 2014; Goswami et al. 2017a). We thus use a 3.5-layer intermediate model, including the barotropic and first- and second-baroclinic modes in the free troposphere and a bulk atmospheric boundary layer (ABL) to simulate BSISO events and illustrate possible underlying mechanisms to explain its behavior as observed in nature. The model, first developed and validated in De La Chevrotière and Khouider (2017), is zonally symmetric, as in Drbohlav and Wang (2007), to focus on the northward-propagating disturbances. To mimic the northward migration of the intertropical convergence zone (ITCZ) during the summer monsoon (Ajayamohan et al. 2014), a background SST resembling the mean summer (JJA), observed Indian Ocean SST climatology is imposed by means of the latent heat flux at the surface of the computational domain.

The new model successfully simulates both the climatological-mean monsoon circulation and northward-moving intraseasonal anomalies. Consistent with observations, the climatological-mean meridional–vertical circulation is characterized by a Hadley-like cell extending over the middle and upper troposphere with strong upward motion at low latitudes of the NH and weak downward motion in the Southern Hemisphere (SH). The northward-moving precipitating events are initiated near the equator, between 5°S and 5°N, propagate northward at the speed of roughly $1°\,\mathrm{day}^{-1}$, and eventually terminate near 20°N. Their vertical structure is characterized by an overturning circulation in the middle and upper troposphere. Unlike earlier findings by Wang and collaborators (e.g., Drbohlav and Wang 2005), the northward propagation of precipitation anomalies here is due to the propagation of positive moisture anomalies in the northward direction, resulting from an asymmetry in the meridional velocity induced by the beta effect. From a moisture-budget perspective, the advection term constitutes an intrusion of dry air into the convection center, while moisture convergence supplies the precipitation sink, somewhat consistent with moisture-mode theories (Chikira 2014; Kim et al. 2014; Wolding and Maloney 2015; Jiang et al. 2018). The asymmetry in meridional advection means more dry air is introduced to the southern side of the convection center and shuts convection there, forcing the whole system to move northward. The northward-propagating BSISO anomalies are initiated near the equator, where competing effects between first-baroclinic divergence and second-baroclinic convergence, induced by the descending branch of the Hadley cell and in situ congestus heating, respectively, take place in the lower troposphere. As the northward-moving precipitating events diminish at higher latitudes, the downward branch of this Hadley-type circulation near the equator also diminish, resulting in the dominant second-baroclinic wind convergence near the equator thanks to the prevailing congestus-type convection. This results in significant midtroposphere moisture convergence, due to the second-baroclinic mode, and the intensification of convection, which then begins to slowly move northward and accelerates when it reaches higher latitudes where the beta effect is stronger. The termination often near 20°N and halfway stalling of these precipitating events occur when the asymmetry in the first-baroclinic meridional winds weakens and when the negative moisture gradient to the north of the convection center becomes too strong as the anomaly approaches the imposed warm pool boundary.

The paper is organized as follows. Section 2 reviews the model equations and the multicloud parameterization as well as the data used for the imposed SST profile. Section 3 presents the numerical simulation results where both the mean climatology and the northward-propagating BSISO anomalies are presented and their physical features analyzed. A detailed budget of the moisture equation is given and analyzed in section 4, where the beta-induced asymmetry is explained in light of a simplified dry shallow-water wave model. The initiation, stalling, and termination mechanisms are discussed in section 5, while the sensitivity of the simulated northward-propagating BSISOs to the SST distribution is reported in section 6. A summary discussion is given in section 7.

2. Data, model, and methodology

a. *The zonally symmetric multicloud model with boundary layer dynamics*

The multilayer dynamical core used here is derived in De La Chevrotière and Khouider (2017), based on the hydrostatic Boussinesq equations on the equatorial β plane for the free troposphere with zonal symmetry, which are written below in dimensional units of tropical synoptic-scale dynamics, where the first-baroclinic gravity wave speed of $c \approx 50\,\mathrm{m\,s^{-1}}$ is the reference scale for horizontal velocity components, the equatorial Rossby deformation radius of $L_e = \sqrt{c/\beta} \approx 1500\,\mathrm{km}$ is the horizontal length scale, and the eddy turn over time $T_e = \sqrt{c\beta} \approx 8.33\,\mathrm{h}$ is the time scale, with β the gradient of the Coriolis parameter at the equator. The temperature fluctuations scale is set to $\sim$15 K so that both β and the background potential temperature stratification $d\overline{\theta}/dz$ are unity in those new dimensional units. The height of the troposphere $H_T = 16\,\mathrm{km}$ is used as a reference vertical coordinate scale and $W = H_T/T_e \approx 53\,\mathrm{cm\,s^{-1}}$ is used as a vertical velocity scale. We have

$$\frac{\partial u}{\partial t} + v\frac{\partial u}{\partial y} + w\frac{\partial u}{\partial z} - yv = \mathcal{S}^u, \tag{1a}$$

$$\frac{\partial v}{\partial t} + v\frac{\partial v}{\partial y} + w\frac{\partial v}{\partial z} + yu = -\frac{\partial p}{\partial y} + \mathcal{S}^v, \tag{1b}$$

$$\frac{\partial \theta}{\partial t} + v\frac{\partial \theta}{\partial y} + w\frac{\partial \theta}{\partial z} + w = \mathcal{H}^\theta + \mathcal{S}^\theta, \tag{1c}$$

$$\frac{\partial p}{\partial z} = \theta, \quad \text{and} \tag{1d}$$

$$\frac{\partial v}{\partial y} + \frac{\partial w}{\partial z} = 0, \tag{1e}$$

where $\mathcal{S}^u$ and $\mathcal{S}^v$ represent momentum turbulent drag, and $\mathcal{H}^\theta$ and $\mathcal{S}^\theta$ stand for diabatic heating and radiative cooling, respectively. The zonal derivative $\partial/\partial x$ is not included in the equations for the zonal symmetric condition.

Equations (1a)–(1e) are projected onto the barotropic and first- and second-baroclinic modes following the Galerkin expansion:

$$\begin{pmatrix}\mathbf{u}\\ p\end{pmatrix}(y,z,t) = \begin{pmatrix}\mathbf{u}_0\\ p_0\end{pmatrix}(y,t) + \begin{pmatrix}\mathbf{u}_1\\ p_1\end{pmatrix}(y,t)C_1(z) + \begin{pmatrix}\mathbf{u}_2\\ p_2\end{pmatrix}(y,t)C_2(z), \quad \text{and} \tag{2}$$

$$\begin{pmatrix}\theta\\ w\end{pmatrix}(y,z,t) = \begin{pmatrix}0\\ w_0\end{pmatrix}(y,t) + \begin{pmatrix}\theta_1\\ w_1\end{pmatrix}(y,t)S_1(z) + \begin{pmatrix}2\theta_2\\ w_2\end{pmatrix}(y,t)S_2(z), \tag{3}$$

where $C_j(z) = \sqrt{2}\cos(jz)$ and $S_j(z) = \sqrt{2}\sin(jz)$ are the vertical structure functions of the first-baroclinic ($j = 1$) and second-baroclinic ($j = 2$) modes, respectively. The resulting three fully coupled shallow-water-like systems are strongly coupled with each other through nonlinear advection terms.

Equations (1) are supplemented with the multicloud parameterization diagnostic and prognostic equations, bulk ABL dynamics, and moist thermodynamics equations, obtained by averaging the primitive equations over the thin ABL constant height and an equation for the vertically averaged moisture (Waite and Khouider 2009). To close the bulk ABL dynamic equations, continuity of pressure and vertical velocity, at the ABL top interface, is assumed. This, in particular, provides dynamical coupling between the ABL dynamics and the free-tropospheric barotropic flow (Waite and Khouider 2009; De La Chevrotière and Khouider 2017).

For the sake of streamlining, the dynamical model equations are listed in Table 1, where the barotropic and first- and second-baroclinic variables are indexed by 0, 1, and 2, respectively, while the ABL variables are indexed by the letter b. Notice the presence of cross-indexed terms in the free-tropospheric equations. In addition to continuity of pressure and vertical velocity, the ABL and free-tropospheric dynamics are coupled through the entrainment and detrainment turbulent mixing terms because of shallow cumulus activity and downdrafts, which appear on the right of the ABL equations in Table 1, involving variables such as E, E_u, $\Delta_t u$, and M_d. As can be seen from Table 2, similar terms appear as momentum damping in the free troposphere (closure equations of S_u and S_v) and as a source of midtropospheric moisture. Table 2 lists all the closure equations of the multicloud model with ABL dynamics (Waite and Khouider 2009). Worth noting, the diabatic heating terms on the right of the θ_1 and θ_2 equations involve convective heating due to congestus, deep, and stratiform heating (H_c, H_d, and H_s, respectively) corresponding to the main three cloud types that characterize organized tropical convective systems (Johnson et al. 1999; Khouider and Majda 2006b) and radiative cooling terms consisting of background climatological values $Q_{R,j}$, $j = 1$, 2 and Newtonian cooling terms.

The values of the parameters and model constants are listed in Table 3. More details on this multicloud model with ABL dynamics are found in Waite and Khouider (2009) and De La Chevrotière and Khouider (2017).

To handle this highly nonlinear, nonconservative, and nonhyperbolic system, without adding the artificial hyperviscosity that is typically implemented in geophysical fluid dynamics simulations to stabilize the numerical scheme, the equations in Table 1 are solved numerically using an operator splitting method where the dynamical equations are divided into a conserved system, a hyperbolic system, and a nilpotent system of

TABLE 1. Governing equations for all physical variables in the ABL, barotropic, and first- and second-baroclinic modes in the free troposphere. The notation $D_0/Dt = \partial/\partial t + v_0\partial/\partial y$ stands for the advection by barotropic meridional velocity and $D_b/Dt = \partial/\partial t + v_b\partial/\partial y$ stands for the advection by the ABL meridional velocity. The momentum and potential temperature differences between two heights are denoted by the notations $\Delta_s\varphi \equiv \varphi_s - \varphi_b$, $\Delta_t\varphi \equiv \varphi_b - \varphi_t$, and $\Delta_m\varphi \equiv \varphi_b - \varphi_m$, where s, b, and m represent the surface, ABL, and middle troposphere, respectively. The parameter δ is the ratio between the ABL and free-tropospheric heights.

Variable	Governing equation
u_0	$\frac{D_0u_0}{Dt} + \frac{\partial(u_1v_1)}{\partial y} + \frac{\partial(u_2v_2)}{\partial y} - \sqrt{2}(u_1 + u_2)\frac{\partial v_0}{\partial y} - yv_0 = \mathcal{S}_0^u$
v_0	$\frac{D_0v_0}{Dt} + \frac{\partial(v_1v_1)}{\partial y} + \frac{\partial(v_2v_2)}{\partial y} - \sqrt{2}(v_1 + v_2)\frac{\partial v_0}{\partial y} + yu_0 = -\frac{\partial p_0}{\partial y} + \mathcal{S}_0^v$
u_1	$\frac{D_0u_1}{Dt} + v_1\frac{\partial u_0}{\partial y} + \frac{\sqrt{2}}{2}\left(v_1\frac{\partial u_2}{\partial y} + v_2\frac{\partial u_1}{\partial y} + 2u_2\frac{\partial v_1}{\partial y} + \frac{1}{2}u_1\frac{\partial v_2}{\partial y}\right) - \left(\frac{1}{2}u_1 + \frac{8}{3}u_2\right)\frac{\partial v_0}{\partial y} - yv_1 = \mathcal{S}_1^u$
v_1	$\frac{D_0v_1}{Dt} + v_1\frac{\partial v_0}{\partial y} + \frac{\sqrt{2}}{2}\left(v_1\frac{\partial v_2}{\partial y} + v_2\frac{\partial v_1}{\partial y} + 2v_2\frac{\partial v_1}{\partial y} + \frac{1}{2}v_1\frac{\partial v_2}{\partial y}\right) - \left(\frac{1}{2}v_1 + \frac{8}{3}v_2\right)\frac{\partial v_0}{\partial y} + yu_1 = \frac{\partial \theta_1}{\partial y} + \mathcal{S}_1^v$
θ_1	$\frac{D_0\theta_1}{Dt} - \frac{\partial v_1}{\partial y} + \frac{\sqrt{2}}{2}\left(2v_1\frac{\partial \theta_2}{\partial y} - v_2\frac{\partial \theta_1}{\partial y} + 4\theta_2\frac{\partial v_1}{\partial y} - \frac{1}{2}\theta_1\frac{\partial v_2}{\partial y}\right) + \left(\frac{1}{2}\theta_1 - \frac{8}{3}\theta_2\right)\frac{\partial v_0}{\partial y} + \sqrt{2}\,\frac{\partial v_0}{\partial y} = H_d - Q_{R,1} - \frac{1}{\tau_D}\theta_1$
u_2	$\frac{D_0u_2}{Dt} + v_2\frac{\partial u_0}{\partial y} + \frac{\sqrt{2}}{2}\left(v_1\frac{\partial u_1}{\partial y} - u_1\frac{\partial v_1}{\partial y}\right) + \left(\frac{2}{3}u_1 - \frac{1}{2}u_2\right)\frac{\partial v_0}{\partial y} - yv_2 = \mathcal{S}_2^u$
v_2	$\frac{D_0v_2}{Dt} + v_2\frac{\partial v_0}{\partial y} + \left(\frac{2}{3}v_1 - \frac{1}{2}v_2\right)\frac{\partial v_0}{\partial y} + yu_2 = \frac{\partial \theta_2}{\partial y} + \mathcal{S}_2^v$
θ_2	$\frac{D_0\theta_2}{Dt} + \frac{\sqrt{2}}{4}\left(v_1\frac{\partial \theta_1}{\partial y} - \theta_1\frac{\partial v_1}{\partial y}\right) - \frac{1}{4}\frac{\partial v_2}{\partial y} + \frac{1}{2}\left(\frac{4}{3}\theta_1 + \theta_2\right)\frac{\partial v_0}{\partial y} + \frac{\sqrt{2}}{4}\frac{\partial v_0}{\partial y} = \frac{1}{2}\left(H_c - H_s - Q_{R,2} - \frac{1}{\tau_D}\theta_2\right)$
q	$\frac{D_0q}{Dt} + \frac{\partial}{\partial y}[(\tilde{\alpha}_1v_1 + \tilde{\alpha}_2v_2)q + \tilde{Q}_1v_1 + \tilde{Q}_2v_2 - \tilde{Q}_0v_0] - (\kappa - 1)q\frac{\partial v_0}{\partial y} = -\mathcal{P} + \mathcal{S}^q$
θ_{eb}	$\frac{D_b\theta_{eb}}{Dt} = -E\Delta_t\theta_e - M_d\Delta_m\theta_e + \frac{1}{\tau_e}\Delta_s\theta_e - Q_{Rb}$
θ_b	$\frac{D_b\theta_b}{Dt} = -E\Delta_t\theta - M_d\Delta_m\theta + \frac{1}{\tau_e}\Delta_s\theta - Q_{Rb}$
u_b	$\frac{D_bu_b}{Dt} - yv_b = -E_u\Delta_tu - C_dUu_b$
v_b	$\frac{D_bv_b}{Dt} + yu_b = -\frac{\partial p_b}{\partial y} - E_u\Delta_tv - C_dUv_b$
—	Continuity of vertical velocity: $\frac{\partial v_0}{\partial y} = -\delta\frac{\partial v_b}{\partial y}$
—	Continuity of total pressure: $p_0 = p_b + \delta\frac{\pi}{2}\theta_b + \sqrt{2}(\theta_1 + \theta_2)$

equations, which are then discretized with appropriate methods. The details are found in De La Chevrotière and Khouider (2017) where the numerical method was developed and validated; the same technique has been used in Khouider and Majda (2005) and Stechmann et al. (2008) for similar nonlinear multimode systems. The equations are solved on a meridional domain extending from 40°S to 40°N using no flow boundary conditions. We used a spatial resolution $\Delta y = 36\,\mathrm{km}$ and a time step $\Delta t = 180\,\mathrm{s}$ to better resolve the fast convective processes.

b. Observed SST profile and the imposed surface latent heat flux

To provide a constant surface latent heat flux for the simple (3.5 layer) zonally symmetric monsoon model used here, we mimic the observed SST over the Indian Ocean during boreal summer. More precisely, the discrepancy between the boundary layer saturation equivalent potential temperature θ^*_{eb} and the background boundary layer equivalent potential temperature $\overline{\theta}_{eb}$, $\Delta_s\theta_e = \theta^*_{eb} - \overline{\theta}_{eb}$ in the model, determines the boundary layer evaporative heating in the form of $(1/\tau_e)(\theta^*_{eb} - \overline{\theta}_{eb})$, and it is thus set to match the observed SST profile. Its strength is set based on the tropical Jordan sounding (Gill 1982) so that its meridional average is close to 10 K, corresponding to the value used to set a radiative–convective equilibrium (RCE) for linear wave analysis of the multicloud model (Khouider and Majda 2006b; Waite and Khouider 2009). We used 35-yr (December 1981–December 2016) monthly means of SST data from NOAA Optimum Interpolation SST, version 2 (OISSTv2), data product (Reynolds et al. 2002), provided by the NOAA/OAR/ESRL/Physical Sciences Division (PSD), Boulder, Colorado (http://www.esrl.noaa.gov/psd). The SST value over land is obtained by a Cressman interpolation. To investigate SST over the Indian Ocean region, all SST values are

TABLE 2. Multicloud and ABL models with closure equations for all forcing terms appearing in the governing equations in Table 1. The primes stand for deviations from the RCE solution. The expression with the superscript plus sign has the same value as that inside the fencing if the latter has positive value and vanishes if its value is negative or zero.

Forcing term	Closure equation
Momentum turbulent drag for barotropic mode	$\mathcal{S}_0^u = \delta E_u \Delta_t u$
Momentum turbulent drag for baroclinic modes	$\mathcal{S}_j^u = \frac{\sqrt{2}\delta}{\tau_\mathcal{T}}\Delta_t u - \frac{1}{\tau_\mathcal{R}} u_j, \quad j = 1, 2$
Velocity jump at the top of the ABL	$\Delta_t \mathbf{u} = \mathbf{u}_b - \mathbf{u}_0 - \sqrt{2}(\mathbf{u}_1 + \mathbf{u}_2)$
Congestus heating	$\frac{\partial H_c}{\partial t} = \frac{1}{\tau_c}(\alpha_c \Lambda Q_c - H_c)$
Deep convective heating	$H_d = (1 - \Lambda) Q_d$
Stratiform heating	$\frac{\partial H_s}{\partial t} = \frac{1}{\tau_s}(\alpha_s H_d - H_s)$
Bulk energy available for congestus convection	$Q_c = \left\{\overline{Q} + \frac{1}{\tau_\mathrm{conv}}[\theta'_{eb} - a'_0(\theta'_1 + \gamma'_2\theta'_2)]\right\}^+$
Bulk energy available for deep convection	$Q_d = \left\{\overline{Q} + \frac{1}{\tau_\mathrm{conv}}[a_1\theta'_{eb} + a_2 q' - a_0(\theta'_1 + \gamma_2\theta'_2)]\right\}^+$
Moisture switch function	$\Lambda = \begin{cases} 1, & \text{for} \quad \Delta_m\theta_e \geq \theta^+ \\ 0, & \text{for} \quad \Delta_m\theta_e \leq \theta^- \\ \text{linear and continuous,} & \text{for} \quad \theta^- < \Delta_m\theta_e < \theta^+ \end{cases}$
Precipitation rate	$\mathcal{P} = \frac{2\sqrt{2}}{\pi} H_d$
Moisture source	$\mathcal{S}^q = \delta E \Delta_t \theta_e + \left(\delta M_d + \frac{\partial v_0}{\partial y}\right)\Delta_m \theta_e$
Equivalent potential temperature at the top of the ABL	$\theta_{et} = \kappa q$
Equivalent potential temperature at the middle troposphere	$\theta_{em} = q + \frac{2\sqrt{2}}{\pi}(\theta_1 + \alpha_2\theta_2)$
Total downdraft mass flux	$M_d = \left\{D_c + \frac{\partial v_b}{\partial y}\right\}^+$
Convective updraft mass flux	$M_u = \frac{1}{\alpha_m} D_c$
Mass flux velocity from large-scale and convective downdrafts	$D_c = m_0\left[1 + \frac{\mu}{\overline{Q}}(H_s - H_c)\right]^+$
Moist thermodynamic turbulent entrainment velocity at top of ABL	$E = \left(M_u - M_d + \frac{\partial v_b}{\partial y}\right)^+$
Momentum turbulent entrainment velocity at top of ABL	$E_u = \left(\frac{1}{\tau_T} + \frac{\partial v_b}{\partial y}\right)^+$

averaged over the longitude range of 60°–90°E at different seasons. The resulting profiles are plotted in Fig. 1a. Figure 1b shows the imposed surface latent flux profile, mimicking the JJA-observed profile. The horizontal black line marks the benchmark RCE value. The explicit expression of the imposed SST distribution (K) reads as follows:

$$\Delta_s \theta_e = \begin{cases} 8e^{-a_0(y-y_1)^2} + 8 & \text{if} \quad y \leq y_1 \\ 16 & \text{if} \quad y_1 < y \leq y_2, \\ 8e^{-a_0(y-y_2)^2} + 8 & \text{if} \quad y \geq y_2 \end{cases} \qquad (4)$$

where $a_0 = 2.0$ is the coefficient controlling the meridional gradient of SST and $y_1 = -0.37$ (5°S) and $y_2 = 1.48$ (20°N) denote, respectively, the southern and northern ends of the warm pool. Note that despite the idealized mathematical formula, the resulting SST gradient at the northern and southern edges remains roughly the same as in the observed profile shown in Fig. 1a. As reported in section 6, the results presented here are not sensitive to mild variations in the SST gradient parameters.

3. Northward-propagating intraseasonal signals and monsoon-like climatology

As summarized in Table 3, the multicloud parameterization employs a large set of parameters. Compared to the standard values established in Khouider and

TABLE 3. Constants and parameters in the multicloud and ABL models.

Parameter	Value	Description
H_T	16 km	Height of the free troposphere
h_b	500 m	ABL depth
δ	0.03125	Ratio of ABL depth to height of the troposphere
κ	1.25	Ratio of moisture at the top of ABL to that in the free troposphere
$\overline{Q}$	1.11 K day^{-1}	Heating potential at RCE
Q_{R1}	1 K day^{-1}	Longwave first-baroclinic radiative cooling rate
Q_{R2}	-0.226 K day^{-1}	Longwave second-baroclinic radiative cooling rate
Q_{Rb}	5.11 K day^{-1}	ABL radiative cooling rate
m_0	5.12×10^{-3} m s^{-1}	Downdraft velocity reference scale
α_c, α_s	0.22, 0.25	Congestus, stratiform adjustment coefficient
a_0	3	Contribution of θ_1 to deep convective heating anomalies
a_1	0.45	Contribution of θ_{eb} to deep convective heating anomalies
a_2	0.55	Contribution of q to deep convective heating anomalies
γ_2	0.1	Relative contribution of θ_2 to deep convective heating anomalies
a_0'	1.7	Contribution of θ_1 to shallow heating anomalies
γ_2'	2	Relative contribution of θ_2 to shallow heating anomalies
α_2	0.1	Relative contribution of θ_2 to θ_{em}
μ	0.25	Contribution of convective downdrafts to M_d
τ_c, τ_s	1, 3 h	Congestus, stratiform adjustment time scales
τ_{conv}	2 h	Convective time scale
θ^-, θ^+	10, 20 K	Moisture switch threshold values
τ_D	50 days	Newtonian cooling time scale
τ_R	75 days	Rayleigh drag time scale
τ_T	8 h	Momentum entrainment time scale
τ_e	7.08 h	Surface evaporation time scale
U	2 m s^{-1}	Strength of turbulent velocity
C_d	0.001	Surface drag coefficient
α_m	0.2	Ratio of D_c to M_u
$\tilde{\alpha}_1$	1	First-baroclinic coefficient of nonlinear moisture flux anomaly
$\tilde{\alpha}_2$	0.1	Second-baroclinic coefficient of nonlinear moisture flux anomaly
$\tilde{Q}_0$	1.674 (nondimensional)	Barotropic mode coefficient of background moisture convergence
$\tilde{Q}_1$	0.558 (nondimensional)	First-baroclinic coefficient of background moisture convergence
$\tilde{Q}_2$	0.212 (nondimensional)	Second-baroclinic coefficient of background moisture convergence

Majda (2006b) and Waite and Khouider (2009), only two particular parameters that would largely influence the magnitude and scale selection of precipitation have been tuned here to reach a realistic-looking climatological-mean circulation with significant intraseasonal variability, namely, the congestus adjustment coefficient, which is set to $\alpha_c = 0.22$ (the default is $\alpha_c = 0.25$), and the ratio of moisture at the top of the ABL and the midtropospheric moisture, which is set to $\kappa = 1.25$ (the default is $\kappa = 2$). Starting from a state of rest initial conditions, the equations are integrated for ~1019 days (to time $t = 3000$ in nondimensional units). The solution reaches a statistical equilibrium state within the first 50 days. Because of the comparable magnitude between BSISO and monsoon background circulation (Lau and Waliser 2011), linear analysis by only focusing on the linear terms that describe interactions between mean and anomalous fields should not be used here, as the nonlinear advection terms involving only anomalous fields are as large as the linear terms. Instead, nonlinear analysis of the model results based on the total field is undertaken here, where the monsoon background circulation can still be calculated by taking long-time averaging, and BSISO anomaly fields are simply the residue.

a. Northward propagation

In Fig. 2, we show the Hovmöller diagrams (latitude–time contours) of precipitation during both the first 50 days' transient period and during the statistical equilibrium period of 910–985 days. As we can see, after a transient period of 20 days or so, the dominant precipitation signals get organized into propagating streaks that start near the equator and move northward and die right before they reach 20° latitude, coinciding with the point where the imposed surface latent heat flux in Fig. 1 plunges down. The precipitation streaks repeat roughly every 20 days, about half of the observed BSISO period (Lau and Waliser 2011), corresponding to an average propagation speed of 1° day^{-1} (or 1.29 m s^{-1}).

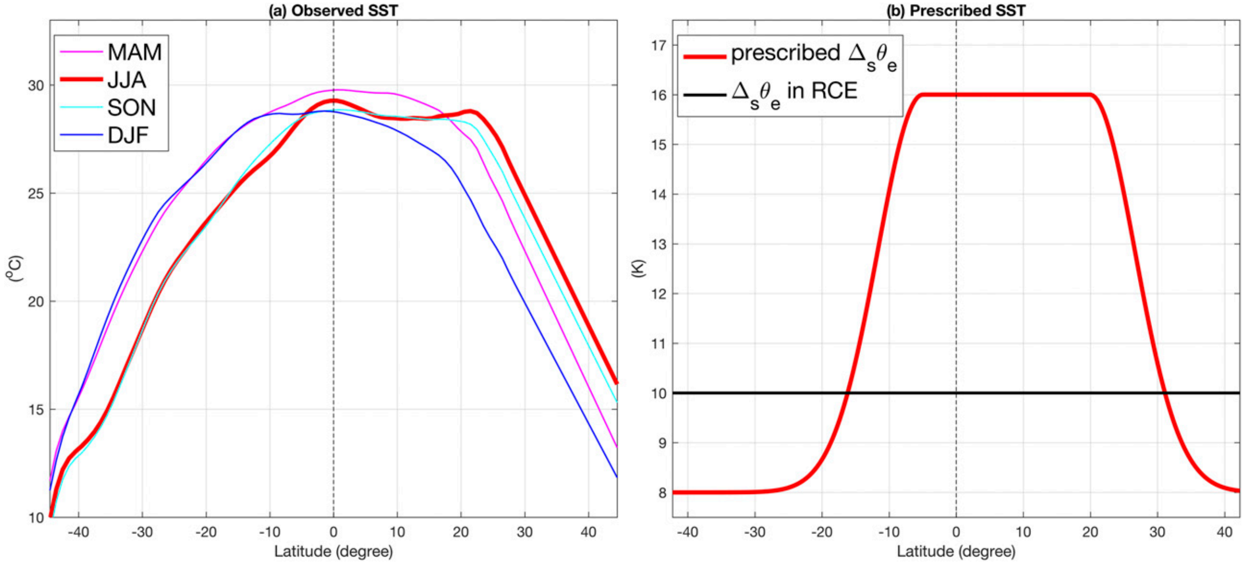

FIG. 1. Meridional profiles of SST over the Indian Ocean monsoon region. (a) Climatological mean of seasonal-mean of observed SST (°C) averaged over the period of July 1981–June 2016 and the longitude range of 60°–90°E, based on the NOAA OISSTv2 data product. The four curves in different colors correspond to different seasons. (b) The prescribed $\Delta_s\theta_e$ (K; red) and its mean value (black). The dashed lines in both panels show the equator.

A closer look reveals that the propagation is actually not constant but undergoes a regime change, which goes through two main phases. The precipitation signal begins moving at low latitudes below 10° at roughly 0.53° day^{-1} and then suddenly accelerates, and its speed becomes 1.12° day^{-1} as indicated by the dashed lines in Fig. 2a. While such regime change is not justified by the flat $\Delta_s\theta_e$ profile in Fig. 1, and perhaps not yet elucidated in observations, it is important for understanding the northward-propagation mechanism. This is one of the main goals here, as it is the focus of section 4.

Figure 2c displays the power spectrum of precipitation in the frequency (meridional) wavenumber domain. There is a clear dominant spectral peak at the 20-day period corresponding to the BSISO-like signals in Fig. 2a, but there are also weaker signals at discrete frequencies, which are signatures of a direct cascade of energy toward smaller scales because of quadratic nonlinear interactions between the various modes of the model. The dominant signal of a 20-day period interacts with itself to produce a 10-days-period signal, which in turn interacts with the 20-day period signal to produce a $1/(1/10 + 1/20) = 6.667$-day signal (the third horizontal strike from the bottom), while the interaction of the 10-day signal with itself produces a 5-day signal, and so on.

We now average in time the numerical solution over the last 500 days of simulation, between 519 and 1019 days, to obtain a climatological background. This background is then removed from the original time-dependent solution to reveal the fluctuations. Figure 3 shows Hovmöller diagrams for the fluctuations of all the prognostic model variables listed in Table 1 as well as the three heating rates H_c, H_d, H_s corresponding to congestus, deep, and stratiform cloud types, with the precipitation contours (in black) overlaid on top of each panel. The name of the variables are indicated on top of each panel. The BSISO-like signal is evident in all zonal velocity fields, including the ABL, barotropic, and first- and second-baroclinic meridional velocity anomalies. However, the barotropic meridional velocity is very weak, while v_b is dominated by high-frequency signals moving in the opposite direction to the main BSISO signal.

The BSISO signal is strongly dominant in the moisture q, deep convective heating H_d, and stratiform heating H_s panels, which are perfectly in phase with precipitation. Because of the slow propagation speed, the imposed 3-h lag between stratiform and deep convection becomes insignificant. Congestus heating presents a negative anomaly along the precipitation path as expected from its design to be disfavored to the advantage of deep convection when the atmosphere is moist. Congestus heating is active during the suppressed phase of the BSISO signal and appears to be carried by the high-frequency/fast-moving waves seen in the v_2 and θ_2 panels, which are also dominant in the θ_{eb} and θ_b anomalies. In essence, the θ_{eb} fluctuations trigger the streaks in congestus

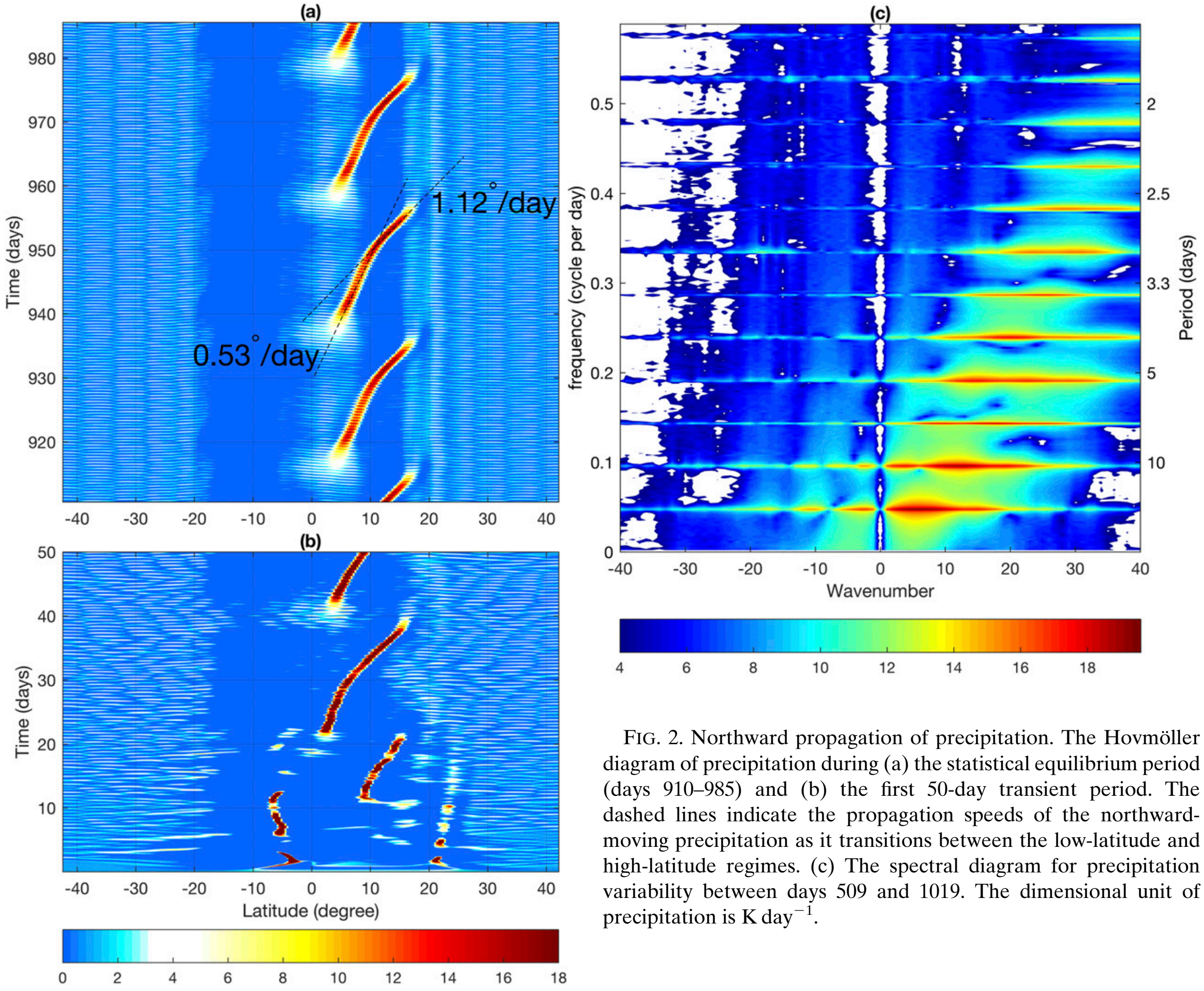

FIG. 2. Northward propagation of precipitation. The Hovmöller diagram of precipitation during (a) the statistical equilibrium period (days 910–985) and (b) the first 50-day transient period. The dashed lines indicate the propagation speeds of the northward-moving precipitation as it transitions between the low-latitude and high-latitude regimes. (c) The spectral diagram for precipitation variability between days 509 and 1019. The dimensional unit of precipitation is K day^{-1}.

heating when the atmosphere is dry, which in turn drive θ_2 and, consequently, second-baroclinic moisture convergence anomalies. However, because the fast waves seem to also weakly precipitate (as seen in the H_d panel), this second-baroclinic convergence is not a significant driver of moistening during the mature phase of the BSISO wave, which is dominated by large-scale first-baroclinic convergence consistent with observations (Hohenegger and Stevens 2013). Nonetheless, as we will see below, congestus preconditioning plays a central role during the initiation phase of the BSISO signals near the equator. In Fig. 3, there is a clear large-scale signature of θ_{eb}, which leads the BSISO precipitation, and evidence of ABL preconditioning prior to deep convection, consistent with observations (e.g., Bellenger et al. 2015). In the equatorial region, this preconditioning occurs several days prior to the initiation of the BSISO event, for instance, day 935 in Fig. 3i.

A noticeable feature in the streaks of the zonal wind component is the positive barotropic shear vorticity, which can be surmised from the westerly wind lagging south of the easterlies, though this cyclonic vorticity gets compensated by contributions from the first- and second-baroclinic vorticities. The former is negative in the upper troposphere, while the latter is negative in the lower and upper troposphere according to their respective $\cos(z)$ and $\cos(2z)$ profiles. The presence of the cyclonic barotropic vorticity is consistent with the simulation of Drbohlav and Wang (2005); arguably, in their case, the positive vorticity does not get compensated with the second-baroclinic mode, since their model does not have one. Drbohlav and Wang (2005) argue that this positive vorticity constitutes the main mechanism for northward propagation by inducing barotropic convergence of moisture within the ABL; however, as we can see from Fig. 3, the large-scale signature is very weak in both v_b and v_0, so, clearly, this is not the mechanism at

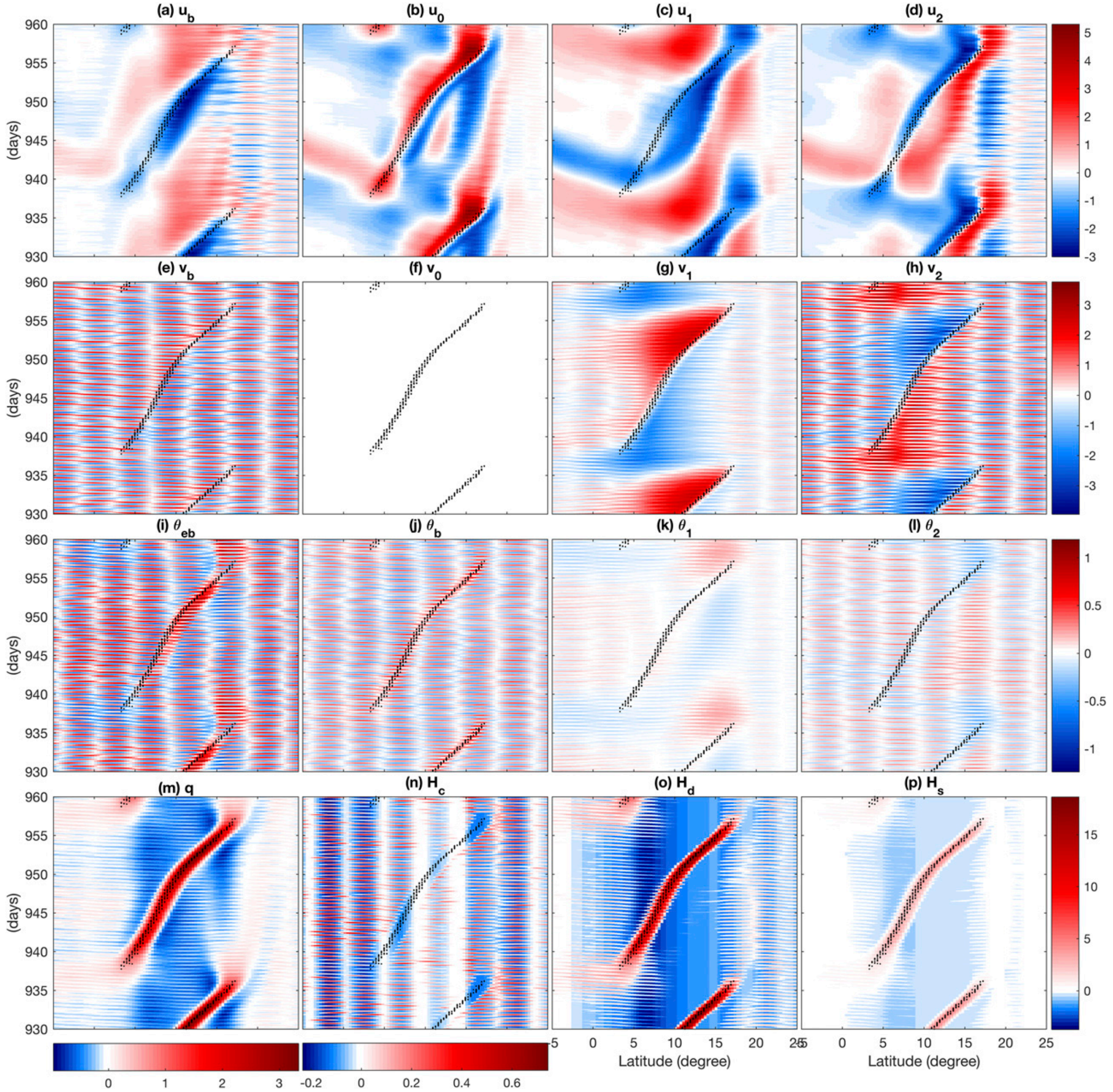

FIG. 3. Hovmöller diagrams for all flow field anomalies (deviation from the climatological mean). (a)–(d) Zonal velocity (m s^{-1}), (e)–(h) meridional velocity (m s^{-1}), and (i)–(l) potential temperature (K) for the (left to right)ABL, barotropic, and first- and second-baroclinic modes. (m)–(p) Moisture (K) and congestus, deep, and stratiform heating (K day^{-1}), respectively. Each row of panels shares the same colorbar at the right-hand side except for (m) and (n), which have their own colorbars at the bottom. The black dots show the latitude of the maximum precipitation anomalies at each time step.

work in the present model. The main mechanisms will be discussed in section 4, as already anticipated.

b. *Circulation patterns and dynamical evolution of the BSISO signals*

We now turn into the dynamical structure of the BSISO-like signal. Compared with the equilibrium stage where the background circulation may be suspected to maintain northward propagation, the dynamical evolution of the northward-moving event at the early stage is informative to illustrate key mechanisms for the northward propagation of each single event before the background circulation is fully established. We begin by plotting in Fig. 4 the structure of the total solution during the early stage of the simulation, focusing on the first event that propagates all the way

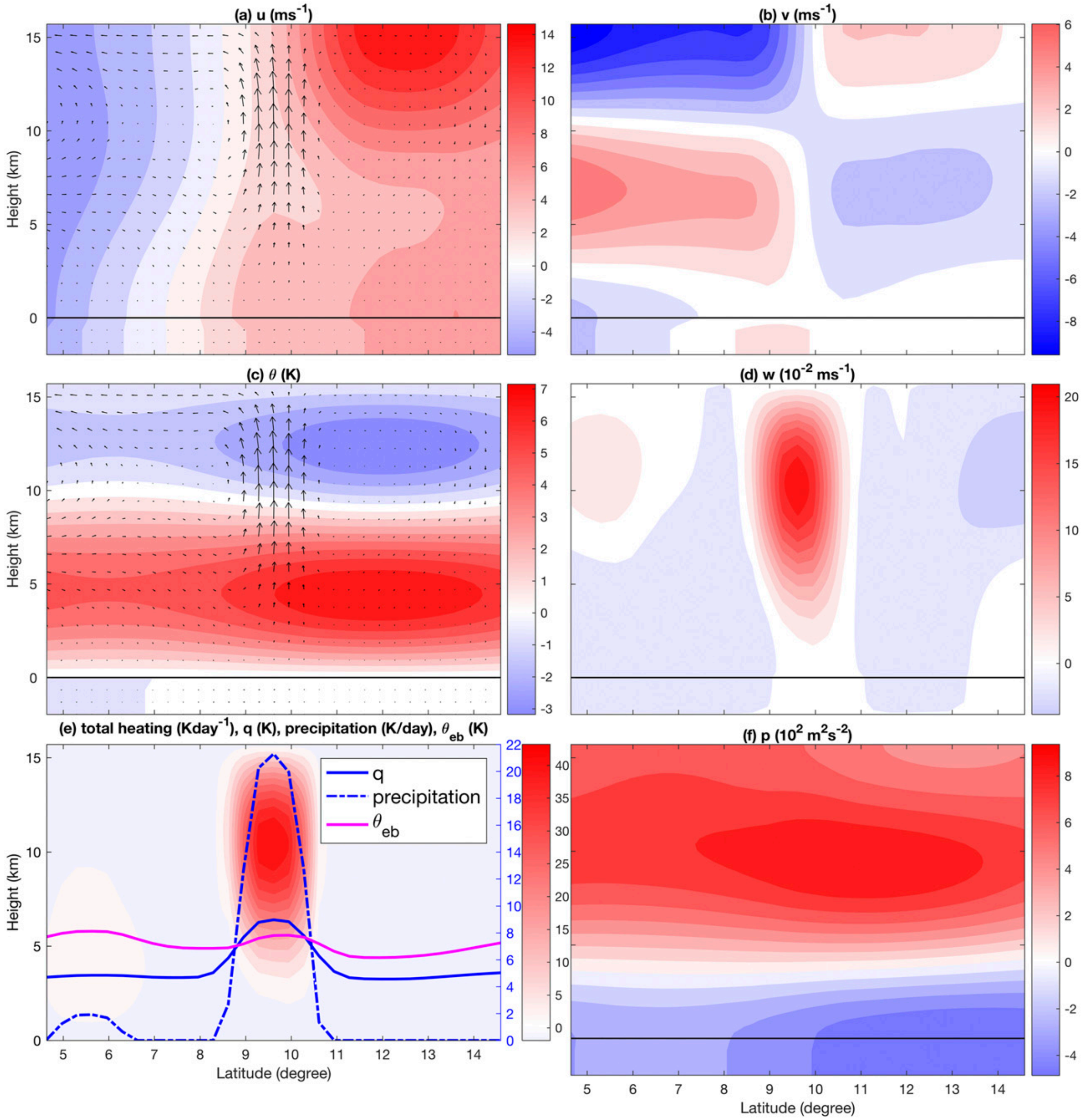

FIG. 4. Meridional circulation at the early stage of the simulation (day 33.3) in the latitude–height diagram, for (a) zonal velocity, (b) meridional velocity, (c) potential temperature, (d) vertical velocity, (e) total heating (color contours), and (f) pressure. The arrows in (a) and (c) show meridional circulation (v, w). In (e), dimensionless value of moisture (solid blue curve), boundary layer equivalent potential temperature (purple), and precipitation (dashed blue curve) are shown by the right axis. The thick black line indicates the interface between free troposphere and ABL. The dimensional units are shown in the titles of each panel.

northward, seen roughly between 20 and 40 days in Fig. 2b. We note that the total dynamical fields have been recovered according to the expansions in Eqs. (2) and (3), and the total heating is accordingly defined as $\mathcal{H} = H_d\sqrt{2}\sin(z) + (H_c - H_s)\sqrt{2}\sin(2z)$. The free-tropospheric profiles are augmented below by their ABL counterparts. Notice the black horizontal line on five of the panels, which marks the ABL top interface and the continuity of the fluid mechanics across this interface.

As we can see from Fig. 4, the northward-propagating BSISO waves have the following characteristics:

1) Positive moisture anomalies are in phase with precipitation and total heating (Fig. 4e).
2) The diabatic heating is top-heavy and slightly skewed southward, a signature of stratiform heating trailing deep convection (Fig. 4e), as in equatorial tropical convective systems (Kiladis et al. 2009; Khouider 2018).
3) A θ_{eb} anomaly, which is slightly leading the convection center, though there is a stronger θ_{eb} peak south of the main signal, between 5° and 6°, which is accompanied by a much weaker precipitation event (Fig. 4e).
4) Upper-tropospheric anticyclonic shear vorticity leads the upward motion (Fig. 4a).
5) A backward-tilted meridional velocity profile resulting in lower-tropospheric convergence and upper-tropospheric divergence, which is highly asymmetric with much stronger winds south of the convection center (Fig. 4b).
6) The vertical velocity is in phase with the precipitation maximum and presents a front-to-rear tilt consistent with the meridional velocity profile (Fig. 4d).
7) Low pressure at low levels (Fig. 4f) and positive temperature anomalies below negative temperature anomalies (Fig. 4c) lead the wave.

In Fig. 5, we plot the climatological mean flow fields in the latitude–height diagram based on the last 500-day model output. As shown in Figs. 5a, 5b, and 5d, there is a counterclockwise circulation cell in the middle to upper troposphere with strong upward motion between the equator and 10°N, followed by a weak downward motion in the Southern Hemisphere. This circulation cell is reminiscent of the local Hadley circulation, which characterizes the Indian summer monsoon. Vertical shear of background zonal winds is mostly significant in the NH between 10° and 20°N. The total heating in Fig. 5e is top-heavy, somewhat more than the propagating event in Fig. 4, indicating the significant contribution from stratiform heating to the mean. The potential temperature mean anomaly is warm in the lower troposphere and cold in the upper troposphere, especially between latitudes 20°S and 30°N, consistent with the individual event structure in Fig. 4. A region of low-level low pressure at high latitudes of the Northern Hemisphere marks a monsoon-like trough climatology. The mean free-tropospheric water vapor is characterized by two strong jumps, one at 20°S and one at 20°N, and a progressive northward sloping in between to reach its maximum near 20°N. Unlike the individual event, the mean moisture maximum is not collocated with the mean precipitation maximum. The accumulation of moisture at northern latitudes can be attributed to the strong northward mean meridional velocity dominating the lower troposphere between roughly 10°S and 10°N. For the sake of simplicity, the mean moisture stratification coefficients ($\tilde{Q}_0$, $\tilde{Q}_1$, $\tilde{Q}_2$) in the moisture equation (Table 1, tenth row) are set to be constant, independent of the latitude. Compared with these, mean moisture stratification, the climatological-mean meridional profile of vertically integrated moisture (deviation from the mean moisture stratification) as shown in Fig. 5e, varies dramatically, reflecting the significant impact of SST on the total background moisture. However, since only the first-baroclinic mode seems to play a major role in the northward-propagation mechanism, the aforementioned simplification is not relevant since these drastic changes in the mean are well represented. The mean zonal velocity is mainly barotropic with a baroclinic signature and a double reversal from westerlies to easterlies to westerlies, in the Northern Hemisphere, consistent with the southerly wind shear prevailing over the summer Indian monsoon trough.

A composite of the anomalous flow fields, with respect to the mean circulation shown in Fig. 5, is presented in Fig. 6. To obtain the composite solution, we averaged the flow anomalies along the curve in the space–time domain following the precipitation maximum, between days 935 and 955, that is, focusing on the corresponding propagating event in Fig. 2a. Such a 20-day average ignores some phase changes for each single field during this period (e.g., relative strength of easterlies and westerlies of v_1 in Fig. 3g), but highlights the important phase relation among different fields. As we can see, this anomalous wave disturbance has many common features with the total solution in Fig. 3, but it has also a few major differences. In particular, the maximum precipitation anomalies in Fig. 6e are about 2 times stronger than those of the climatological-mean precipitation in Fig. 5e, consistent with the dominant magnitude of intraseasonal precipitation anomalies (see Fig. 2.3a in Lau and Waliser 2011) and the climatological-mean precipitation (see Fig. 2.1d in Lau and Waliser 2011) in observation. In contrast, the meridional velocity anomalies in Fig. 6b have a similar maximum magnitude as the climatological mean in Fig. 5b, resembling the realistic strength of anomalous meridional winds (see Figs. 2.5a,b in Lau and Waliser 2011) and mean meridional winds (see Fig. 2c in Wang and Fan 1999) in observation. Among the common features, we can enumerate the correlation of precipitation with anomalous moisture perturbation and θ_{eb} anomalies (although weak; note the 0.1-K units). The skewed θ_{eb} profile is a consequence of ABL drying due to stratiform-induced downdrafts in the wake of the wave. We also have backward-tilted

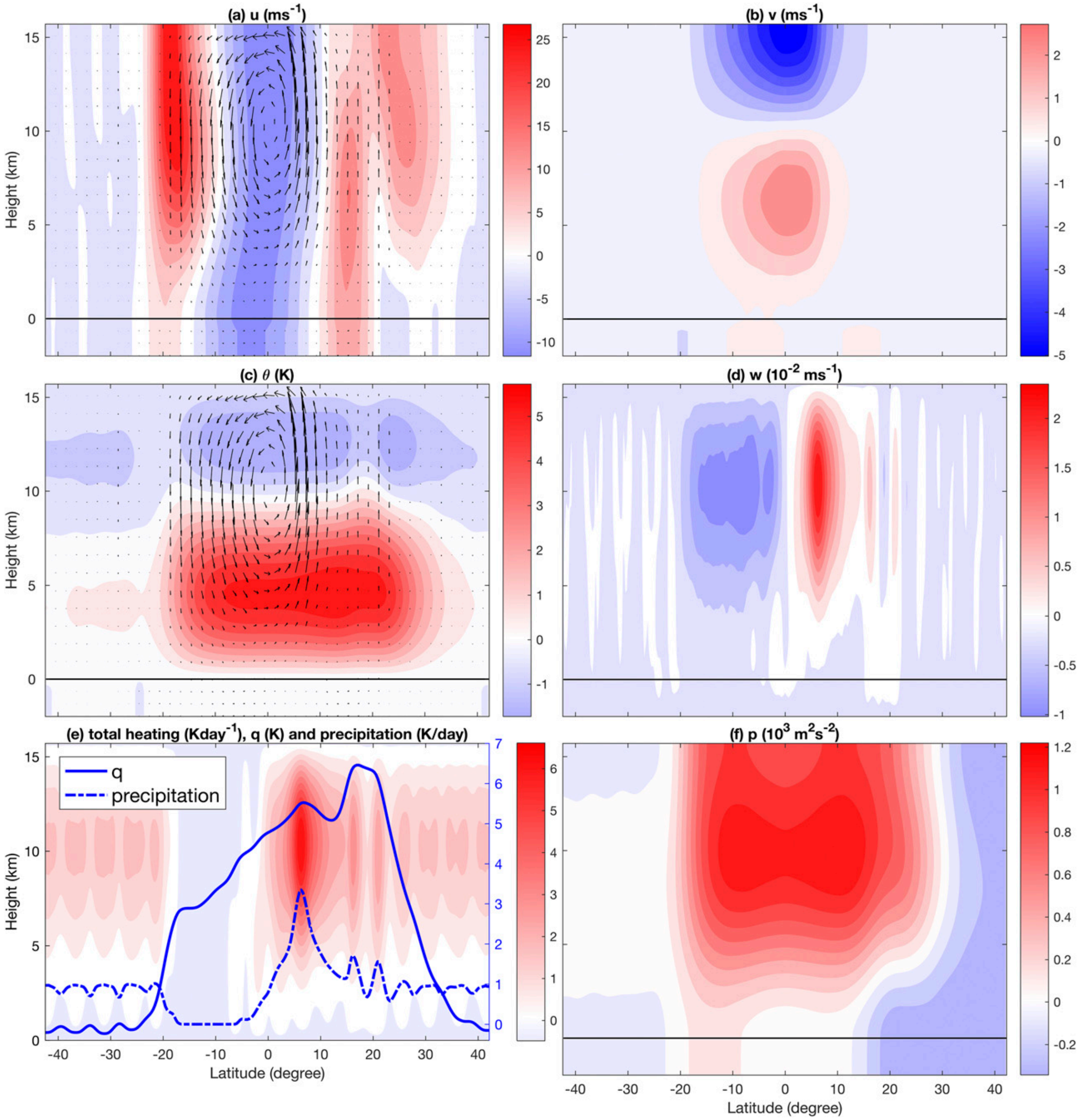

FIG. 5. As in Fig. 4, but for climatological-mean circulation averaged over the period (days 509–1019).

vertical velocity fields with convergence below and divergence aloft and upward motion in phase with the convection. However, unlike the total wave solution in Fig. 2, there is a significant positive shear vorticity ($\omega = -\partial u/\partial y$) in the middle troposphere, though it is far from being simply barotropic.

There is a significant capping by negative vorticity near the top of the domain. The meridional wind appears to be less asymmetric and even somewhat stronger in the northern half of the wave. The potential temperature plot features anomalously warm air topped by cold air north of the convection center, whereas warm temperature sits on top of cold temperature within the convection center. This feature is consistent with equatorial convectively coupled waves and the MJO (Kiladis et al. 2009; Khouider 2018). Moreover, from Fig. 6f, we have a positive pressure perturbation below a negative one ahead of the wave followed by low-level low pressure and upper-level high pressure in hydrostatic balance with the potential temperature in Fig. 6c.

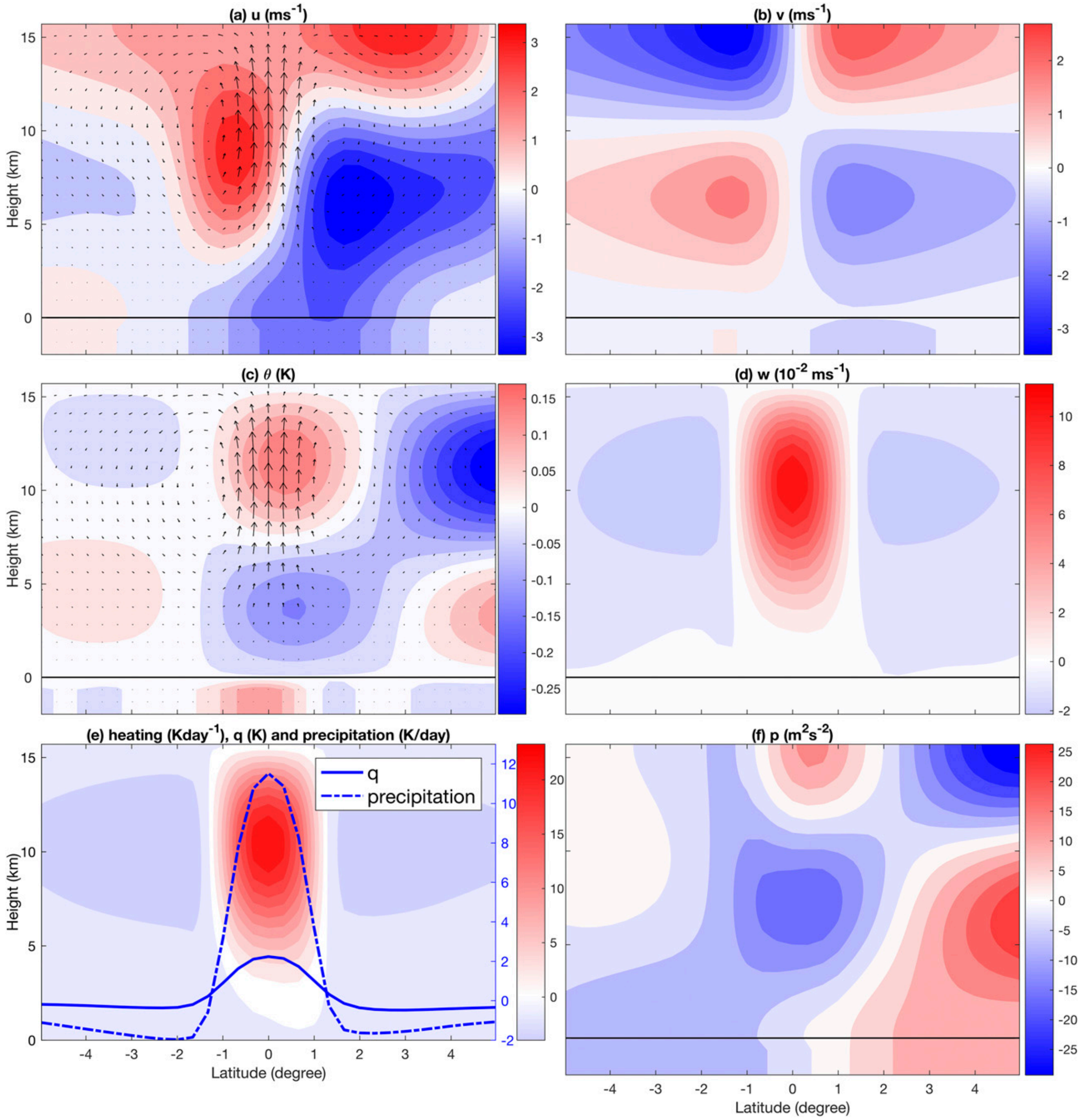

FIG. 6. As in Fig. 4, but for vertical structure of composite flow field anomalies (deviation from the climatological mean) correlated with the northward-propagating precipitation between days 935 and 955 in the latitude–height diagram. The center latitude (0°) corresponds to the latitude where the maximum precipitation is located.

This indicates, in particular, that the wave is mainly baroclinic in nature and the barotropicity is all carried by the mean flow. So the buildup of the positive barotropic vorticity in front of the wave (if there is one) cannot be the driver of the northward propagation in the current model as reported in aforementioned earlier studies.

There is no doubt that the environment plays a role in the wave motion; if the wave could propel itself, it cannot be through the buildup of positive barotropic vorticity. A more appropriate mechanism will be discussed below after we present a detailed budget analysis for the moisture and meridional momentum equations. Contrary to the mean driven-wave fluctuation point of view, our analysis below is based on that the full nonlinear wave solution and the physics of the wave fluctuation (Fig. 5) alone cannot lead to the same conclusive arguments. Specifically, the maximum precipitation anomalies in Fig. 6e are about 2 times more than those in the climatological mean in Fig. 5e. It is those northward-propagating events with strong anomalous fields that further strengthen the mean circulation. Of course, this mean circulation could also influence each single northward-propagating event in return. This two-way feedback between mean circulation and waves plays a central role in the mechanisms proposed here for BSISO initiation, propagation, and termination.

4. Propagating mechanism of northward-moving precipitating events

a. Moisture-budget analysis

The governing equation for vertically integrated moisture in the free troposphere is given in the tenth row of Table 1. Following Khouider and Majda (2006a), the tropospheric moisture equation for q is derived from the bulk water vapor budget equation by assuming a background moisture profile that decays exponentially in height and consistently projecting all terms into the first- and second-baroclinic modes. Particularly, in terms of the first- and second-baroclinic modes, the vertical velocity is given by the meridional gradient of meridional velocity through the continuity equation in Eq. (1e), $w_j = -(1/j)(\partial v_j/\partial y)$, $j = 1, 2$. As shown by Fig. 3m, the northward propagation of precipitation anomalies is closely tied to the movement of moisture anomalies. Thus, moisture tendency terms could illustrate key factors that drive the northward propagation of the whole system, reminiscent of the moisture-mode theory (Chikira 2014; Kim et al. 2014; Wolding and Maloney 2015; Jiang et al. 2018).

In Fig. 7, we plot the profiles of all the tendency terms for the free-tropospheric moisture for two different events, one corresponding to an early stage of the BSISO event when it is still near the equator, below 10°N (slow propagation regime), and the other at higher latitudes, above 10°N, when the BSISO propagation speed gets accelerated (fast propagation regime). We note that the nonlinear moisture flux terms, corresponding to the barotropic and first-baroclinic modes, have been divided into convergence, $q\partial v_j$, and advection, $v_j\partial q$, $j = 0, 1$, terms. Before digging into differences between these two cases, we focus on some of the main common features. In both cases, the total time tendency (thick black curve) of moisture $\partial q/\partial t$ is characterized by positive anomalies to the north and negative tendency to the south of the precipitation maximum (thick red curve), which is consistent with the northward propagation of the wave disturbance. The main moisture source comes from the terms $-q\partial(\tilde{\alpha}_1 v_1)/\partial y$ and $-\partial(\tilde{Q}_1 v_1)/\partial y$ corresponding to the first-baroclinic convergence of moisture anomalies and moisture background, respectively. The combination of these two terms by themselves balance the sink of moisture due to precipitation and the second-baroclinic divergence of background moisture, $-\partial(\tilde{Q}_2 v_2)/\partial y$, as they seem to be perfectly in phase with each other. We notice that the barotropic convergence (thin pink line) is practically zero, and the second-baroclinic convergence is, interestingly, a moisture sink. The latter is due to the prevalence of stratiform heating, which induces low-level divergence in the second-baroclinic mode. The meridional profiles of all moisture convergence terms are perfectly symmetric about the maximum precipitation. Thus, moisture convergence by either barotropic or baroclinic modes cannot be the reason for the northward propagation of the moisture disturbance and ultimately the convectively coupled wave.

In addition to the second-baroclinic divergence and precipitation, the major moisture sinks include meridional advection, $-v_1\partial(\tilde{\alpha}_1 q)/\partial y$. Among these three processes, only the first-baroclinic meridional advection term shows substantial meridional asymmetry to be able to induce the northward propagation of moisture anomalies. It is the moisture source S^q (thin orange curves) due to turbulent mixing and evaporation that tends to moisten the neighboring area both to the north and south of the precipitation maximum, but the first-baroclinic meridional advection term substantially consumes moisture to the south and has negligible magnitude to the north. In detail, the moisture source S^q in Table 2 includes two parts, one of which comes from boundary layer evaporation due to turbulent mixing and the other from free-tropospheric rain evaporation due to downdrafts. This moisture source closure does not directly involve surface winds, unlike the wind-induced surface heat exchange (WISHE) mechanism (Emanuel 1987). WISHE theory for the MJO requires stronger surface evaporation on the eastern side of the disturbances, whereas the moisture source in Fig. 7 is symmetric about the convection center. It is the first-baroclinic advection other than the moisture source that breaks the meridional asymmetry and promotes the northward propagation. Thus, we argue that the latter is the main physical mechanism that induces northward propagation of the BSISO signals in the present model simulation, mainly through the intrusion of relatively dry air from the southern flank of the convection center, forcing the whole system to move northward where the environment is less hostile for new convection. We note that the curves

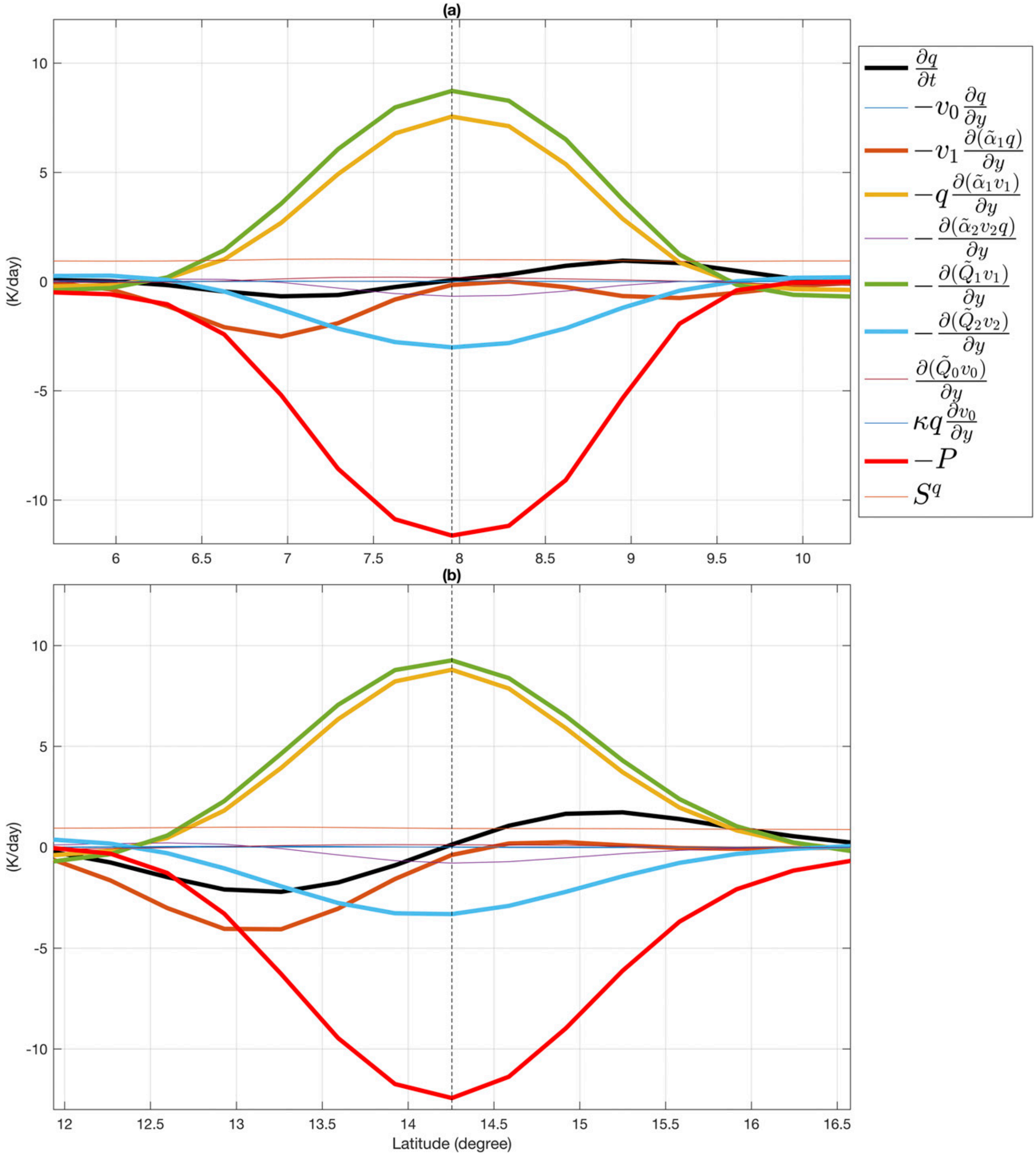

FIG. 7. Moisture-budget analysis of a composite event for all terms appearing in the free-tropospheric moisture equation based on 24 northward-propagating events during the second 500-day period. The cases when the maximum precipitation is located at (a) 7.9° and (b) 14.25°N. The curves in different colors correspond to different terms as shown in the legend. Only the latitude range in the neighborhood of the maximum precipitation is shown here. All dominant terms are shown in thick curves. The dashed lines indicate the latitude with the maximum precipitation.

in Fig. 7 correspond to the total budget terms and not anomalies, and that the advection asymmetry is consistent with the asymmetry of the meridional velocity seen in Fig. 4, while asymmetry is nonexistent in the fluctuation composite in Fig. 6. Comparing Figs. 7a and 7b, we can see that the main difference is in the magnitude of the first-baroclinic meridional advection asymmetry. The latter is much more significant in

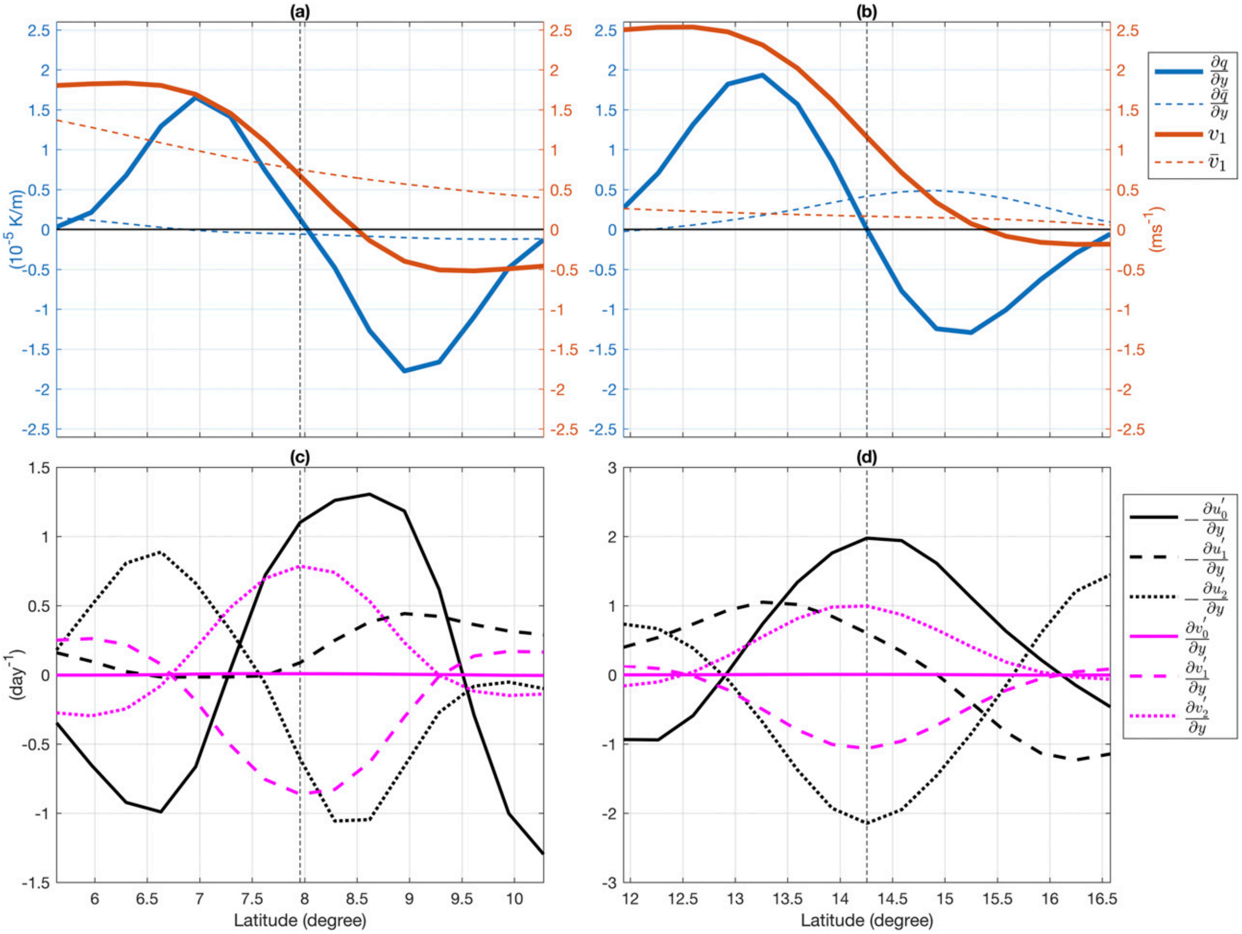

FIG. 8. Meridional profiles of column-integrated moisture gradient, meridional velocity, vorticity, and divergence. (a),(b) Moisture gradient in blue curves and first-baroclinic meridional velocity in red curves. The solid curves are for total values, and the dashed curves are for climatological mean. The solid black line shows zero magnitude. (c),(d) Barotropic and first- and second-baroclinic vorticity anomalies in black curves and divergence anomalies in pink curves. Shown are the cases when the maximum precipitation is located at (a),(c) 7.9° and (b),(d) 14.25°N.

Fig. 7b, consistent with the fact that the wave moves faster north of 10°N.

To dig a bit deeper into this issue, we plot in Figs. 8a and 8b the meridional profiles of total moisture gradient and total first-baroclinic meridional velocity (solid lines) and their respective climatological means (dashed lines) for the cases when the BSISO wave is, respectively, below 10°N and when it moves beyond this latitude. In the low-latitude case in Fig. 8a, the meridional profile of total moisture is mostly symmetric about the precipitation center, while that of meridional velocity is asymmetric with strong southerlies to the south and weak northerlies to the north. The climatological-mean moisture gradient in Fig. 8a is relatively much weaker. Although the v_1 velocity anomalies in the low-latitude case are actually dominated by northerlies to the north, the mean v_1 velocity is significant and overall positive, carrying the asymmetry in the total meridional wind around the precipitation maximum, necessary for the northward propagation. In this sense, the background flows play a major role in meridional moisture transport at the early stage of northward-propagating events. As already anticipated, such strong southerlies south of the precipitation maximum bring dry air into the convection core and force the convection to move to the north. For the high-latitude case in Fig. 8b, on the other hand, the v_1 asymmetry is much stronger, while the meridional gradient of moisture also shows some asymmetry. The asymmetry in the moisture gradient is attributed to the persistence of a background moisture gradient in the mean climatology at those latitudes, consistent with the mean moisture profile in Fig. 5; however, the mean v_1 velocity is weak and the asymmetry of the total v_1 field is mainly attributed to the asymmetry of the v_1 anomaly

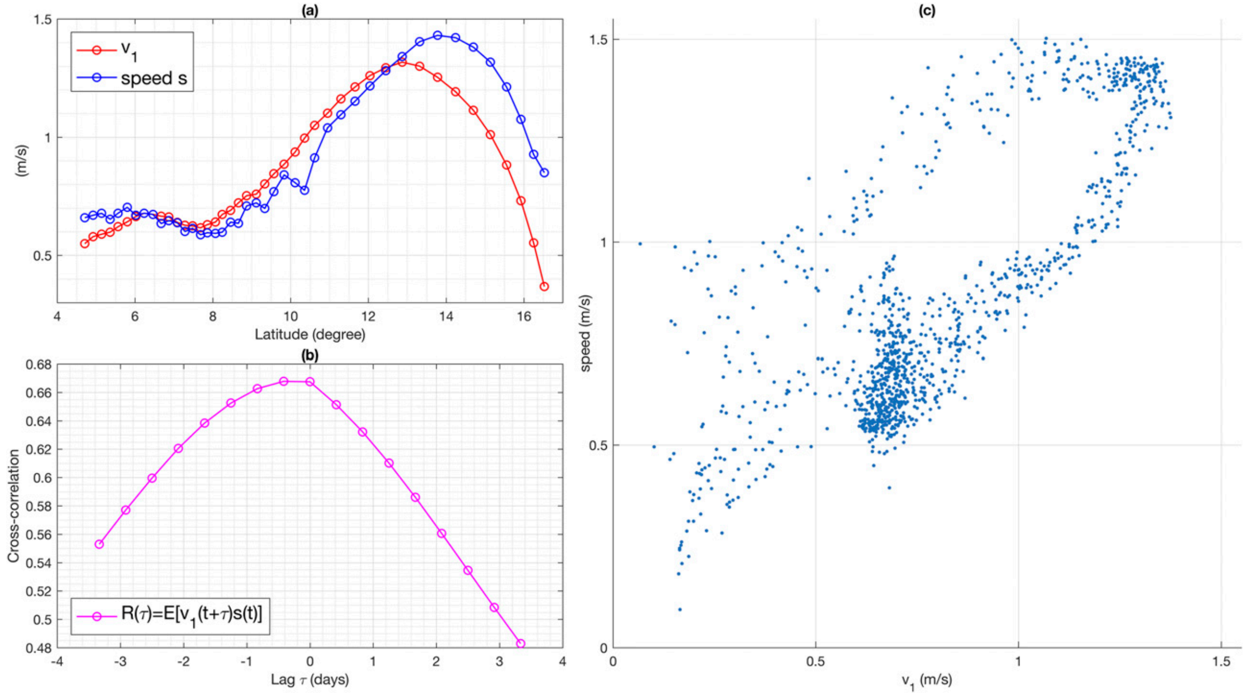

FIG. 9. The phase relation between local-mean first-baroclinic meridional velocity v_1 and propagation speed s of the maximum precipitation. (a) Magnitude when the maximum precipitation reaches each latitude after equal time intervals. (b) Cross correlation between v_1 and s. (c) The scatterplot for all sample snapshots during 24 northward-propagating events. Here, v_1 is averaged over a 4.64° latitude range centered about the maximum precipitation.

field. Also, as shown in Figs. 8a and 8b, both the first-baroclinic meridional velocity v_1 and the moisture gradient $\partial q/\partial y$ have anomalous fields of comparable magnitude as their climatological-mean fields, indicating the substantial contribution from the nonlinear term involving those anomalous fields, $-v_1'\partial(\tilde{\alpha}_1 q')/\partial y$, to the total first-baroclinic meridional moisture advection, $-v_1\partial(\tilde{\alpha}_1 q)/\partial y$. This is a key feature captured by this nonlinear model but would not be captured by the linearized models used in previous studies.

Previous studies (Jiang et al. 2004; Drbohlav and Wang 2005, 2007) had emphasized the role of positive barotropic vorticity anomalies in inducing barotropic convergence, which translates into ABL moisture convergence, north of the convection center and eventually lead to the northward propagation of precipitation. To check this hypothesis more closely, we plot in Figs. 8c and 8d the meridional profiles of vorticity and divergence anomalies. It is particularly interesting to note that the barotropic vorticity anomaly, $-\partial_y u_0'$, does have about a 0.7° northward lead in Fig. 8c but it is mainly in phase with the precipitation maximum in Fig. 8d. If at times barotropic cyclonic vorticity may appear to lead the northward-moving BSISO signals, this feature is not as universal as the asymmetry in the advecting v_1 wind reported above. More importantly, the barotropic wind divergence is close to zero; thus, the ABL convergence mechanism is not present here.

To further show evidence of the relevance of the asymmetry in the first-baroclinic velocity for the northward propagation of the BSISO events, we introduce the average first-baroclinic meridional velocity in the vicinity of the precipitation maximum corresponding to the northward-propagating BSISO events, as

$$\bar{v}_1(y_t) = \frac{1}{y_0}\int_{y_t - y_0/2}^{y_t + y_0/2} v_1(y,t)\,dy, \tag{5}$$

where y_t is the point of maximum precipitation and $y_0 = 4.65°$ is a fixed averaging range, covering a neighboring latitude range around the maximum precipitation of 14 discrete grid points.

In Figs. 9a–9c, we plot the aggregated time mean corresponding to all BSISO events that occurred during the last 500 days of the simulation, roughly 25 events, as a function of latitude, that is, y_t with the mean propagation speed of the BSISO at the corresponding location, the time-lag correlation of $\bar{v}_1(y_t)$ and the BSISO propagation speed $s(y_t)$ and a scatterplot of $\bar{v}_1(y_t)$ with respect to $s(y_t)$. While there is some scattering, it is clear from these figures that these two variables are well correlated, and the regime change of the northward-propagation speed as the BSISO passes beyond some latitude point near 10°N is reflected in the inflection point (a point of minimum speed) seen near 8°, above which both $\overline{v}_1$ and s accelerate to reach its maximum near 14°. We note that $\overline{v}_1$ plunges down first, before the BSISO event terminates at roughly 17°. The latter is somewhat reflected in the lag-correlation plot in Fig. 9b which is, although maximized at $\tau = 0$, highly skewed toward negative lag values hinting to the causal effect of $\overline{v}_1$ on s.

To understand the origin of this asymmetry in meridional wind, we turn to the analysis of the meridional momentum equations. Namely, we will investigate which physical parameter is at the origin of the asymmetry in the first-baroclinic velocity component. According to our experimental setting, including the SST profile in Fig. 1, which is totally flat between latitudes 10°S and 20°N, containing the region where the BSISO event evolves, the only physical parameter susceptible to induce an asymmetry in v_1 is the beta effect. Next, we demonstrate that this is indeed the case in the context of a simple linear dynamical model with an imposed heat source.

b. *Role of beta effect in inducing northward propagation*

We consider the linear first-baroclinic shallow-water equations with an imposed heat source mimicking the convective heating emanating from the BSISO events, which are otherwise completely decoupled from all the other vertical modes, including the ABL. We have

$$\begin{aligned} u_t - yv &= -\alpha u, \\ v_t + yu &= \theta_y - \alpha v, \\ \theta_t - v_y &= Q(y) - \alpha\theta, \end{aligned} \qquad (6)$$

where u, v, and θ are the zonal velocity, meridional velocity, and potential temperature. Here, $Q(y)$ is the imposed heat source having the shape of a Gaussian: $Q(y) = q_0 e^{-[(y-y_0)/L_y]^2}$, where q_0 is the strength of the heating, y_0 its center, and L_y its decaying scale, and $\alpha = 0.02\,\mathrm{day}^{-1}$ is a small damping coefficient taken to be the same for all three equations; it represents the Newtonian cooling and Rayleigh drag inverse time scale in Table 3, which are taken to be equal here for the sake of convenience. We set $y_0 = 10°$ and $L_y = 0.13°$, leading to an effective exponential decay in the heat source of about 2°, while $q_0 = 20\,\mathrm{K\,day}^{-1}$ consistent with the results in Figs. 2, 4, and 6e. Eliminating u and θ from Eq. (6) leads to the following wave-like equation for v:

$$\partial_{tt} v + 2\alpha\partial_t v = \partial_{yy} v - (y^2 + \alpha^2)v + \partial_y Q. \qquad (7)$$

This equation is then solved numerically with centered differences, using homogeneous Dirichlet boundary conditions ($v = 0$). In Fig. 10, we plot the solution at 50 and 100 days of integration on top of its counterpart when the Coriolis parameter is set to zero; that is, the term $y^2 v$ on the right-hand side is dropped. As we can see, the main difference between the two solutions is that the former is asymmetric about the heating center, while the latter is perfectly symmetric. The explanation for this behavior is embarrassingly simple. The Coriolis term $-y^2 v$ acts as an extra damping term for gravity waves, whose magnitude in dimensionless units is much larger than that of $-\alpha^2 v$. For the specific latitude 10°, the dimensionless value of the latitude y under the length scaling, 1500 km, is 0.741. Even if we consider a relatively strong Rayleigh drag scale of 1–10 days (Romps 2014), the dimensionless value of the parameter α under the time scaling, 8.3 h, would be only 0.346–0.035. Correspondingly, the ratio between the Coriolis term $-y^2 v$ and the drag term $-\alpha^2 v$ would be on the order of 4.6–448.2, reflecting the dominant role of the Coriolis term. In the steady state when the solutions reach equilibrium, this damping term $-(y^2 + \alpha^2)v$ arising from the Coriolis force and Rayleigh drag is directly balanced by the second derivative of meridional velocity, $\partial_{yy} v$, and the gradient of the heat source, $\partial_y Q$. A shorter (longer) drag time scale results in a larger (smaller) value of α, which reduces (increases) the magnitude of v. However, the significant meridional asymmetry would not be changed, as long as the Coriolis term dominates the drag term. Notice the wavy character of the 50-day solutions. Since y is larger to the north, there is more damping there.

It is worthwhile noting that the solution in Fig. 10 is quantitatively sensitive to the domain size at the location of y_0 and more importantly to the damping rate, but it remains qualitatively robust, as long as the two boundaries are kept at an equal distance from the heat source. Because of the complex nonlinearity in the multicloud model, as seen in Table 1, it will be hard to draw more analogies with the northward propagation of the BSISO signals presented here, besides the fact that the asymmetry in v_1 originates from the asymmetry in the damping effect. Obviously, in a full 2D model, the Coriolis effect will simply transfer energy from the meridional velocity into the zonal-propagating waves instead of dissipating it, but the end result will most likely be similar, as more energy will be drawn out of v at higher latitudes, that is, north of the convection center, because Poincaré waves with the same wavenumber would have higher frequencies at larger $f(=\beta y)$ parameter values. This simple shallow-water model in Eq. (6) captures the linear governing equations for the

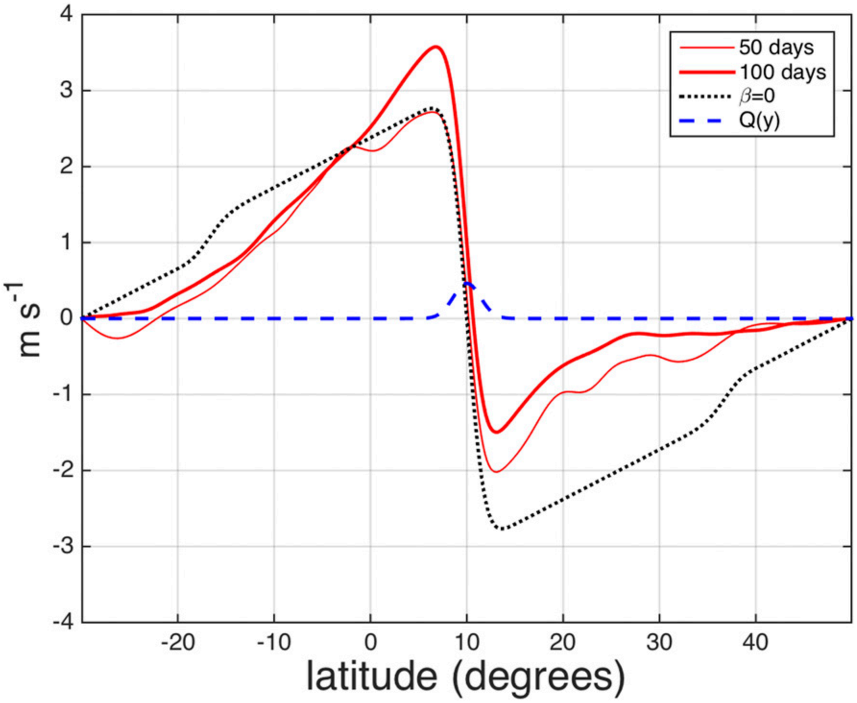

FIG. 10. Solution of the wave equation in Eq. (7) at 50 (thin), 100 days (solid), and without the Coriolis gradient parameter (dots). The dashed line in the background is the imposed steady-heating profile throughout the simulation.

first-baroclinic mode in equatorially trapped dynamics on the β plane. If the Coriolis force is ignored, the reduced governing equation for v in Eq. (7) does allow northward- or southward-propagating gravity waves as the intrinsic meridionally propagating modes. As shown by Eq. (6), the overall effect of the Coriolis force lies in kinetic energy transfer between the zonal and meridional winds. On the β plane, this energy exchange is disproportional between lower and higher latitudes. Thus, the coherent structures associated with meridionally propagating modes will be destroyed, resulting in limited propagation distance off the equator (Majda et al. 2015). Besides, zonally propagating Rossby waves that rely on the meridional gradient of the Coriolis force are excluded here because of the zonally symmetric geometry.

c. *Cause and effect of northward propagation*

We now summarize the main physical processes leading to northward propagating of the BSISO anomalies. 1) Northward propagation is due to the northward movement of moisture anomalies due to the interplay between the symmetric convergence of moisture, which itself results from the induced convective heating, and the asymmetric moisture advection. 2) The asymmetric meridional advection by the first-baroclinic meridional velocity induces dry-air intrusions to the south of moisture anomalies, which make the southern flank of the anomaly unfavorable to new convection, and hence convection is shifted northward. 3) The asymmetric meridional advection is mainly contributed by the asymmetric first-baroclinic meridional velocity v_1, especially at low latitudes. 4) The asymmetry in v_1 results from the beta effect as gravity waves are damped at a higher rate north of the disturbance; this may seem an artifact of the zonally symmetric setting as illustrated above. In a more realistic three-dimensional setting, Poincaré waves at higher latitudes have higher frequencies, especially those with small zonal wavenumbers. As such, energy will be transferred more quickly to smaller scales and thus dissipated at a higher rate north of the precipitation maximum.

5. Initiation and termination of BSISO events

Another issue of great interest is the initiation of the BSISO events in the vicinity of the equator. As shown in Fig. 3, positive precipitation anomalies are generally triggered at low latitudes of the Northern Hemisphere as the preceding northward-propagating BSISO terminates at high latitudes. Through moisture-budget analysis, once again, we would like to figure out the dominant effects that cause the triggering and intensification of convection during the BSISO initiation.

Figure 11a shows the moisture-budget analysis where all terms appearing in the free-tropospheric moisture equation are plotted separately as functions of time. To obtain smooth signals, we have taken averaging about the latitude range between 5°S and 5°N. We focus on the period -15 and $+6$ days, relative to the maximum precipitation. As shown by the thick black line, the time tendency of moisture $\partial q/\partial t$ reaches its maximum value one day before the maximum precipitation and has negative values after the maximum precipitation. From Fig. 11a, we can see that the main dominant terms (excluding S^q, which is all the way constant) are the first-baroclinic moisture convergence, associated with both moisture anomalies $[-q\partial(\tilde{\alpha}_1 v_1)/\partial y]$ and background moisture $[-\partial(\tilde{Q}_1 v_1)/\partial y]$ terms, the second-baroclinic moisture convergence $[-\partial(\tilde{Q}_2 v_2)/\partial y]$, and precipitation $\mathcal{P}$, as well as the term S^q, which provides a constant source of moisture. In terms of their phase relation, all these dominant terms are more or less in phase with the maximum precipitation, but the second-baroclinic convergence (thin magenta line), which peaks some 5 days ahead of the precipitation maximum. While it does not seem to induce a positive moisture tendency at this early stage, it does compensate, together with S^q, for the moisture sink due to the first-baroclinic moisture divergence and precipitation.

In Fig. 11b, we make similar plots for the deep, congestus, and stratiform heating rates, H_d, H_c, H_s, as well as the moisture and different components of potential temperature anomalies. Deep heating H_d is mostly in phase with moisture q, although the maximum moisture does lag the maximum deep heating slightly. Also stratiform heating H_s reaches its maximum strength at almost the same time as deep heating, which is consistent with the fact that the stratiform heating lags deep heating through a relaxation time scale of only 3 h. We note that congestus heating H_c is generally suppressed and nearly vanishes during the deep heating period but is active, reaching up to 0.25 K day^{-1}, the rest of the time when deep convection is suppressed. As for potential temperature anomalies, negative boundary layer equivalent potential temperature anomalies θ_{eb} are induced during precipitation, while the boundary layer potential temperature θ_b has warm anomalies. These thermodynamic anomalies are induced by the downdrafts that tend to dry and warm the ABL. Furthermore, both the first- and second-baroclinic potential temperature anomalies (θ_1, θ_2) lead the maximum precipitation. However, positive first-baroclinic potential temperature anomalies θ_1 lead the first increase in precipitation, before day -5. This is essentially a stabilizing mechanism, and thus temperature anomalies cannot be attributed the role of initiating the BSISO events.

The negative first-baroclinic potential temperature anomalies are induced by dry-wave dynamics, while the deep convective heating is merely compensated by convergence as can be surmised from Fig. 11c, which shows meridional profiles of vorticity and divergence fields in the barotropic and first- and second-baroclinic modes. It is interesting to notice that there are positive barotropic vorticity anomalies $(-\partial u_0'/\partial y)$ two days before the maximum precipitation, although the barotropic divergence field $(\partial v_0'/\partial y)$ shows negligible magnitude. As for the baroclinic mode, there are negative first-baroclinic vorticity anomalies preceding the maximum precipitation. More importantly, second-baroclinic convergence with comparable first-baroclinic divergence precedes the intensified precipitation. The second-baroclinic convergence is maintained by the background congestus heating.

Figures 12a and 12b show a life cycle of one BSISO event starting from its initiation as a big blob of convection near the equator and propagates as such until it reaches relatively high latitudes. We note in particular that during the initiation phase (Fig. 12a), when the dominant event is still at the equator, there is a secondary peak in precipitation at roughly 17°N. The latter is a signature of the termination phase of the preceding BSISO event. Moreover, we note that as the main event propagates northward, it starts inducing subsidence near and south of the equator, suppressing the intensification of convection there. However, as this event moves far enough from the equator, equatorial convection starts to intensify (Fig. 12f) before it becomes again dominant (Fig. 12a) and the cycle is closed.

Before we address the issue of termination of the BSISO events, we summarize here the processes leading to the initiation of BSISO convection near the equator. 1) During the suppressed phase, the first-baroclinic divergence and second-baroclinic convergence cancel each other, resulting in a vanishing moisture convergence. 2) The first-baroclinic divergence near the equator is maintained by the intensification of the local Hadley circulation due to the northward-moving precipitating event when it moves to higher latitudes. 3) Once the propagating event moves to higher latitudes and terminates, the first-baroclinic divergence near the equator weakens and the second-baroclinic convergence, which is maintained by the background congestus heating, becomes dominant, resulting in moisture convergence, and precipitation intensifies at the equator, via a positive feedback loop.

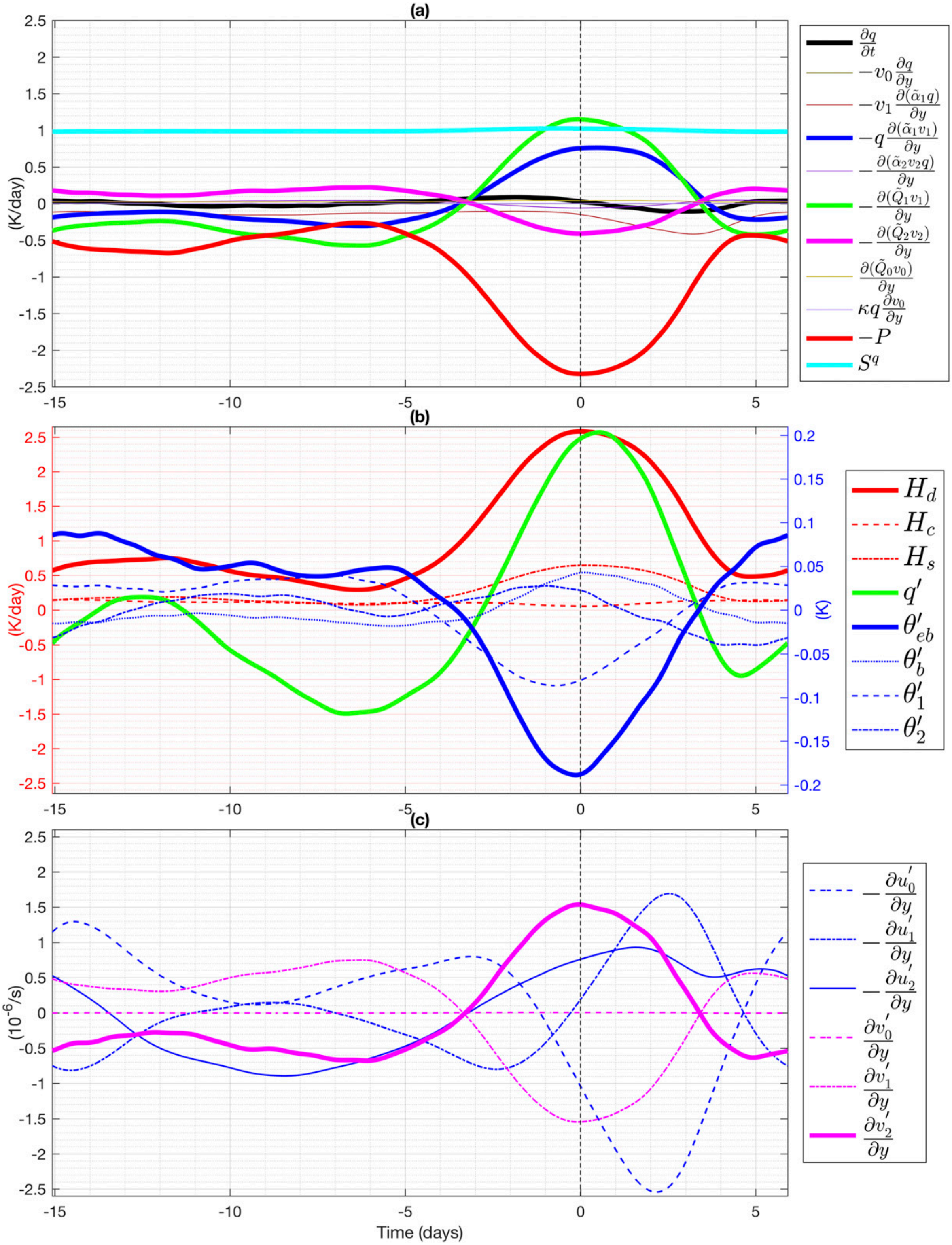

FIG. 11. Time series of (a) moisture-budget terms, (b) heating rates and thermodynamic fields, and (c) vorticity and divergence during the initiation of BSISO events near the equator. All variables have been averaged between 5°S and 5°N, and the resulting time series have been processed by a low-pass filter (removing high-frequency signals in Fourier space and retaining only low-frequency signals), and all signals with periods less than 1 day are filtered out.

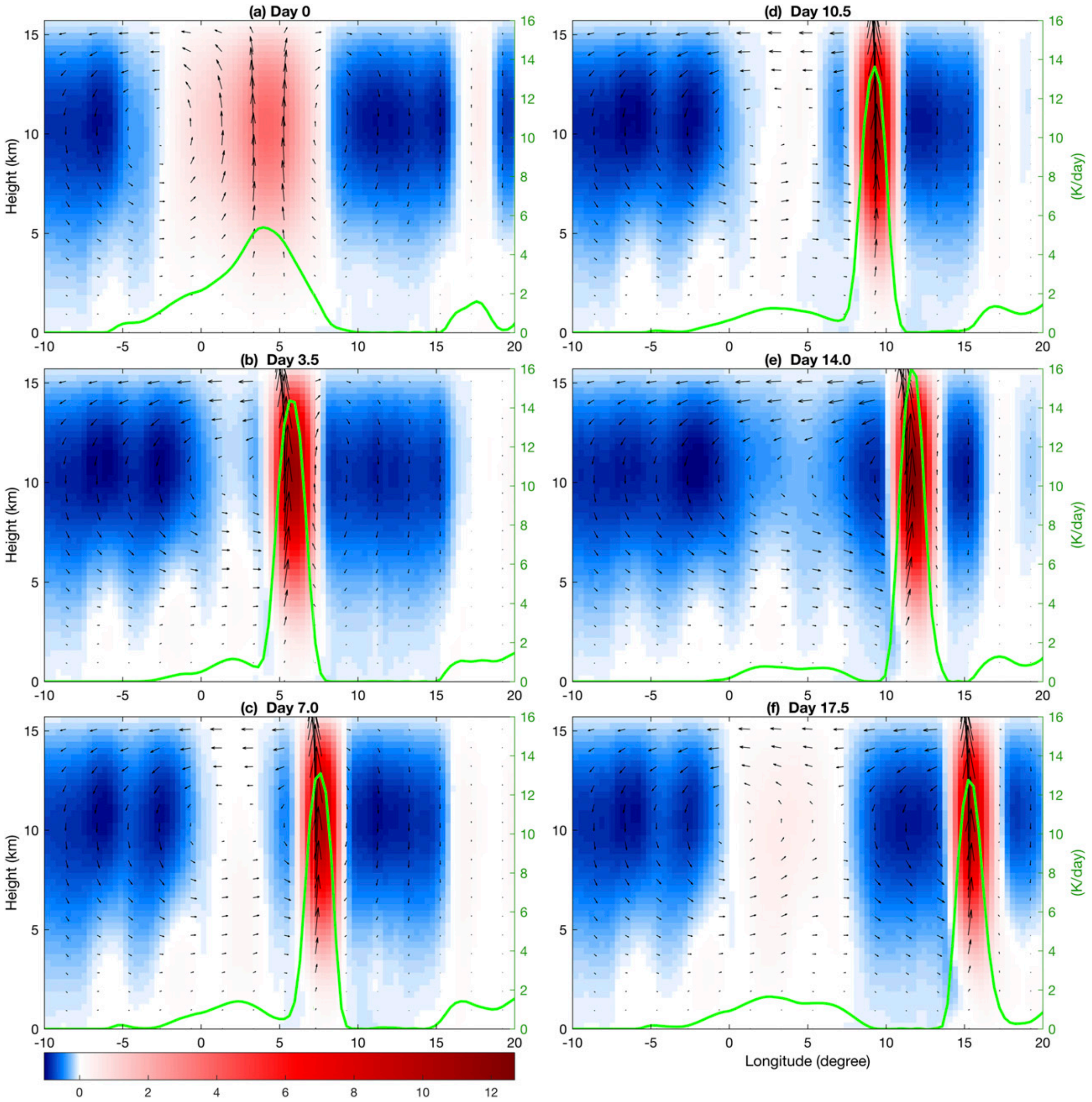
(a) Day 0
(b) Day 3.5
(c) Day 7.0
(d) Day 10.5
(e) Day 14.0
(f) Day 17.5

FIG. 12. Meridional circulation at six different phases in the latitude–height diagram. These six panels are from different phases of the composite life cycle of northward-propagating events with a 3.5-day time interval. Meridional and vertical velocities are shown by arrows, and vertical velocity is also shown by color. The green curve in each panel shows the meridional profile of deep heating with its magnitude indicated by the right axis. The dimensional units of vertical velocity and deep heating are $10^{-2}\,\mathrm{m\,s^{-1}}$ and $\mathrm{K\,day^{-1}}$, respectively.

Figures 13a and 13b show the moisture-budget analysis, all terms appearing in the free-tropospheric moisture equation, at two successive instances during the BSISO life cycle, a few days before its termination. Not surprisingly, the plots in Fig. 13a are very similar to those in Fig. 7b; though redundant, they are kept here to ease the comparison between the mature phase of the BSISO event, represented by Figs. 7b and 13a, and the time when the BSISO event moves to higher latitudes and weakens, represented by Fig. 13b, before it terminates. Notice the weakening of the moisture total tendency north of the convection center and the apparent negative tendency in the vicinity of the precipitation maximum, marked by the vertical dotted line,

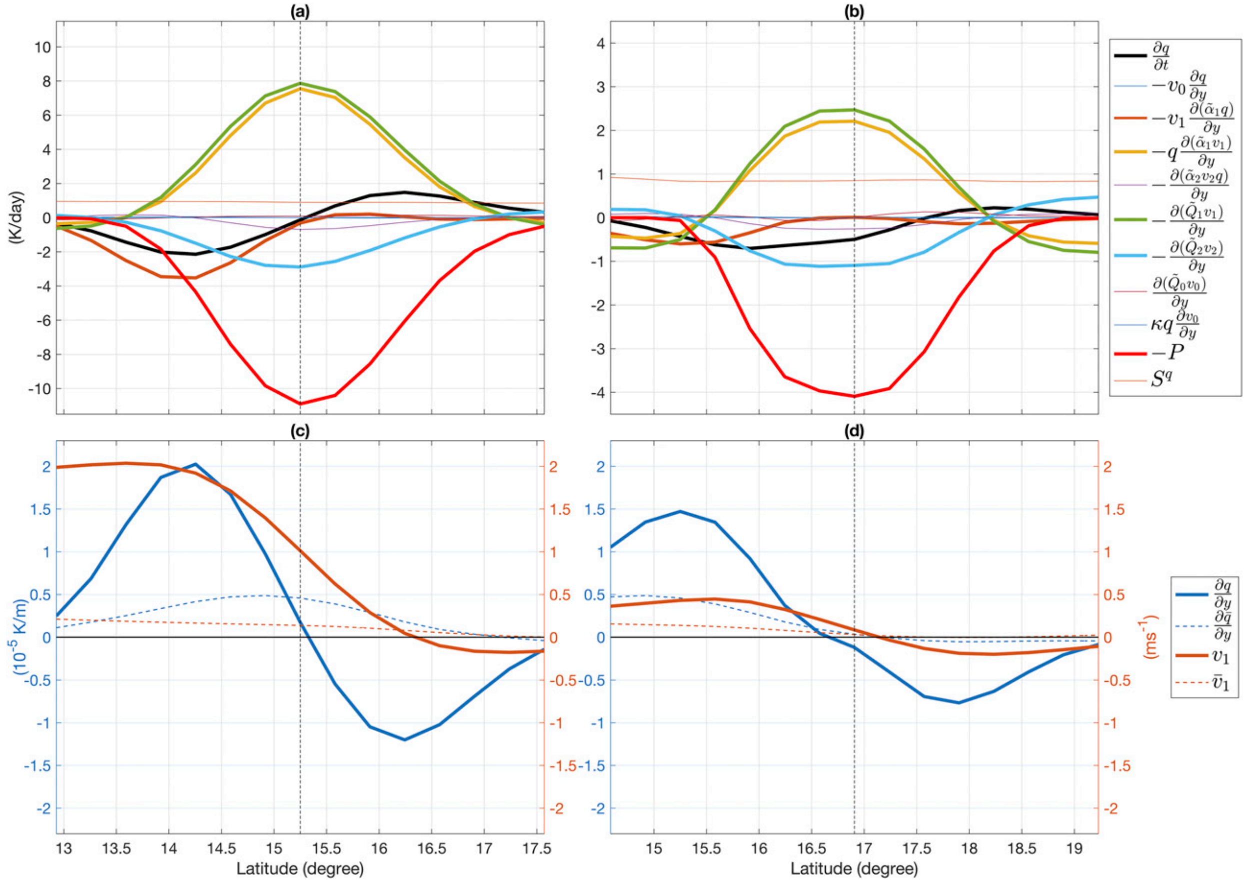

FIG. 13. (a),(b) As in Fig. 7, but for cases when maximum precipitation is located at (a) 15.25° and (b) 16.9°N. (c),(d) The respective equivalents of Figs. 8a and 8b.

in Fig. 13b. Besides this observation, the striking difference between the two panels in Fig. 13 resides in the significant reduction in the (asymmetric) advection of dry air toward the center and, more importantly, in the relatively strong first-baroclinic divergence north of the convection center seen in Fig. 13b. Moreover, all the tendency signals are much weaker at that time (notice the change in scale between Figs. 13a and 13b). The weakening of moisture convergence is probably caused by a weakening of precipitation as the mean moisture gradient starts to decay toward the negatives, as seen in Fig. 13d in comparison with Fig. 13c. As such, the total moisture tendency is much weaker in front of the wave when the BSISO event moves to high latitudes and approaches the edge of the warm SST background, which plunges down at exactly 20°N. As also seen in Fig. 13d, the asymmetry argument in v_1 is still valid; however, the weakening of the wave as a whole makes the average $\bar{v}_1$ in Eq. (5), if it were computed, much weaker, which translates into the stalling of the BSISO event and consequently causing its demise through further weakening via moisture depletion by precipitation. This, in part, explains why the BSISO events do not quite reach the 20°N SST barrier before weakening and terminating.

6. Sensitivity to SST distributions

To investigate the sensitivity of the simulated northward-propagating BSISOs to the SST distribution, we undertake four sensitivity tests (cases 1–4) under the same model setup as before, changing only the prescribed SST distribution. Specifically, case 1 considers a broader warm pool scenario with $y_2 - y_1$ increased by 15% in Eq. (4), while case 2 considers a narrower warm pool decreased by 15%. Case 3 considers a northward-shifted warm pool scenario by adding 2° to both y_1 and y_2, while case 4 considers an opposite scenario by shifting the warm pool 2° southward. These four SST distributions are shown in Figs. 14a and 14d, respectively.

As shown by Fig. 14b, the maximum precipitation intensity in case 1 gets weakened to 4 K day^{-1}. Meanwhile, northward-moving precipitating events are

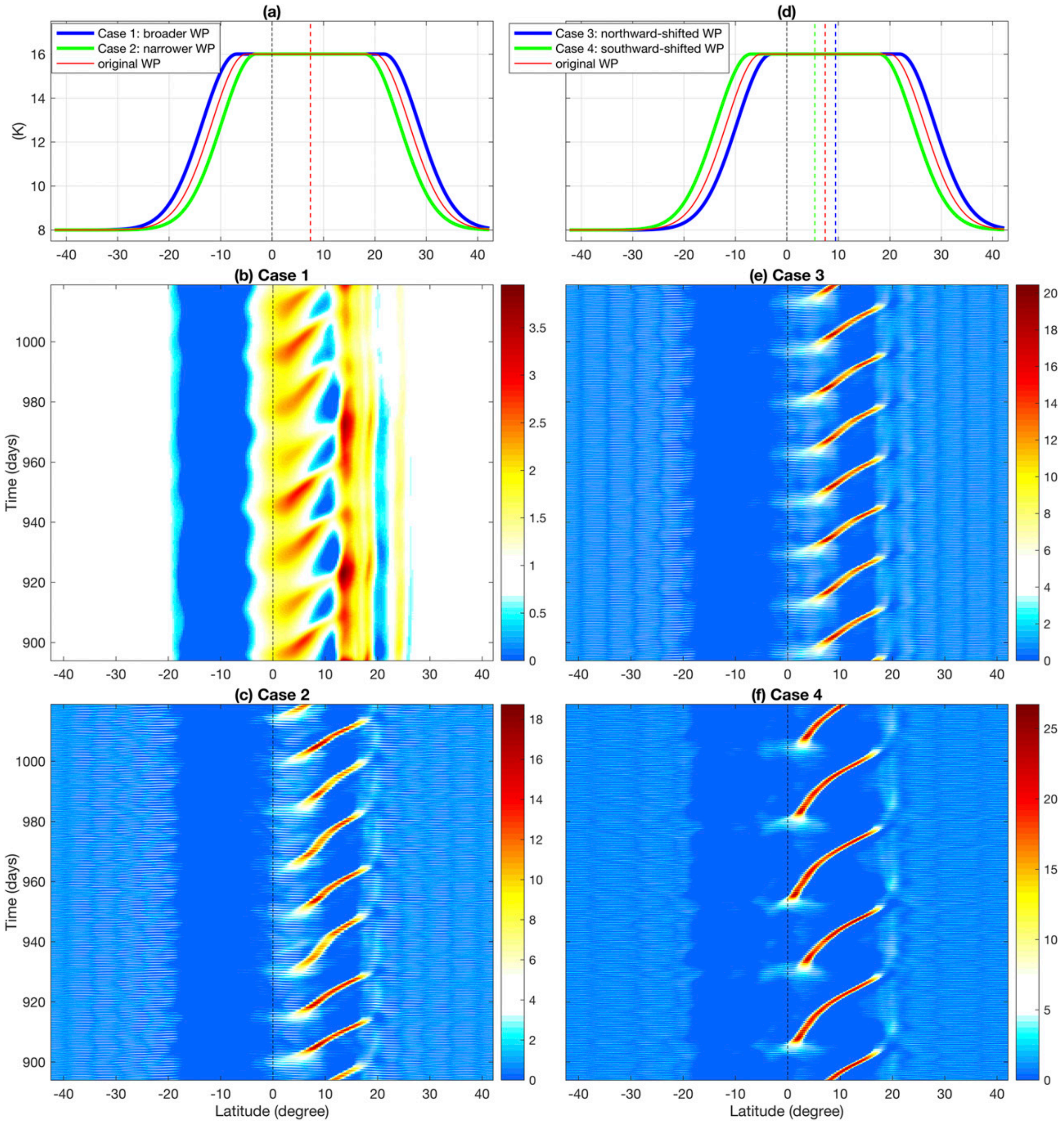

FIG. 14. Hovmöller diagrams for precipitation in sensitivity tests with different SST distributions. (a) SST distributions with the broader warm pool (case 1), narrower warm pool (case 2), and the original one from Fig. 1b. (b),(c) The Hovmöller diagrams of precipitation for cases 1 and 2, respectively. (d)–(f) As in (a)–(c), respectively, but for the northward-shifted warm pool (case 3) and southward-shifted warm pool (case 4). The colored dashed lines indicate the warm pool center for the corresponding case, and the black dashed line indicates the equator. The dimensional units of SST and precipitation are K and K day^{-1}, respectively.

confined between the equator and 10°N. In contrast, case 2 in Fig. 14c features northward-moving precipitating events that are akin to those in Fig. 2a. These events are also present in both case 3 and case 4. Consistent with the northward- and southward-shifted warm pools in Fig. 14d, these events prevail farther north in Fig. 14e than those in Fig. 14f. When compared with case 3, the SST distribution in case 1 differs mainly by its broader warm pool in the SH. It is found (not shown) that the climatological-mean circulation in case 1 is weaker than that in case 3, highlighting its crucial role in promoting northward propagation of precipitation anomalies.

Moreover, sensitivity tests (not shown) regarding the SST meridional gradient at the edge of the warm pool, including both higher- and lower-SST meridional gradients than the observed one in Fig. 1a, show the prevalence of northward-moving precipitating events. Notably, the observed SST in SON in Fig. 1a is very similar to that in the JJA. An extra experiment (not shown) with the prescribed SST for the SON season still features persistent northward-moving precipitating events, confirming the robustness of the physical mechanism.

7. Concluding discussion

Here, we use a nonlinear free-tropospheric model coupled to the multicloud parameterization with ABL dynamics of Waite and Khouider (2009) to simulate the northward-moving BSISO events in order to gain basic understanding about the underlying basic physical mechanisms. The model is based on the zonally symmetric primitive equations, Galerkin projected onto the first three modes of vertical structure: the barotropic mode and the first two baroclinic modes, dynamically and thermodynamically coupled to a bulk (vertically averaged) ABL dynamics. The numerical procedure followed here and its validation as well as it suitability for simulating the monsoon flow are found in De La Chevrotière and Khouider (2017). Zonally symmetric models have been used in the past to study, as in our case, the northward propagation of monsoon precipitation (Drbohlav and Wang 2005) and for the effect of the ABL dynamics on the Hadley cell (Pauluis 2004). Because of its resemblance to the Asian monsoon, the model and results presented here could be applied to the North American monsoon as well (Jiang and Waliser 2009; Jiang and Lau 2008).

The model is forced with an imposed surface latent heat flux based on the observed SST profile over the Indian Ocean summer (JJA) climatology and integrated for roughly 1000 days. Northward-propagating BSISO events, regularly succeeding each other at a period of roughly 20 days and moving at roughly 1° day^{-1}, start to appear after a transient period of nearly the same length. The simulated period (about 20 days) is relatively short compared with the observation (about 40 days). Sensitivity experiments regarding the congestus adjustment coefficient α_c and the ratio of moisture at top of the ABL and the midtropospheric moisture κ show that both parameters would largely influence the scale selection of the northward-propagating events, highlighting the preconditioning moistening effects of congestus convection and moist boundary layer. A further careful calibration about these two parameters may help to improve the period.

Despite the short 20-day period and the 1° day^{-1} propagation speed, the BSISO events have many realistic features, including moisture convergence in phase with the precipitation maximum; a top-heavy heating slightly tilted southward as a result of stratiform heating, which slightly lags deep convection; ABL moisture slightly leading; upper-level shear vorticity leading the wave; a backward-tilted meridional velocity with convergence below divergence aloft, more or less in phase with precipitation, resulting in a tilted upward motion in phase with precipitation; and finally low pressure at low level coinciding with the precipitation center. While these circulation features are more or less in agreement with equatorial-wave dynamics, where the tilted structure is believed to lead to wave propagation, a thorough moisture-budget analysis revealed that the main mechanism responsible for the northward propagation is due to the intrusion of dry air from the southern flank of the wave, induced by an asymmetry in the first-baroclinic meridional velocity. Although dry air is advected from both ends of the convection center, the asymmetry in υ_1 is such that more dry air is pumped from the southern side, making the northern side more favorable to new convection, and thus making the whole disturbance move to the north. We also found that precipitation itself is nearly balanced by moisture convergence, so moisture advection is the sole mechanism responsible for the wave propagation, as we found that the υ_1 asymmetry is statistically correlated with the BSISO propagation speed.

To understand the cause of the asymmetry in the υ_1 velocity, we introduced a toy model reduced to the zonally symmetric first-baroclinic mode with an imposed heating. As demonstrated in Fig. 10, the beta effect alone explains this asymmetry by acting as an asymmetric damping diminishing the strength of the flow response north of the heat source. While the beta damping itself is obviously an artifact of the zonal symmetry, in a fully three-dimensional model this can be contrasted by the fact that zonally propagating Poincaré waves north of the heat source have higher frequencies than those south of the heat source because of the larger f parameter there, thus becoming more effective in transferring energy down to (turbulent) dissipation scales.

Jiang et al. (2004) have proposed the generation of barotropic shear vorticity due to the interactions between the free-tropospheric baroclinic and barotropic modes and the mean flow as the main mechanism for northward propagation by inducing ABL convergence indirectly through the production of upper-level divergence. In this paper, although both the vertical shear of the mean flow (see Fig. 5) and the northward-displaced barotropic vorticity (see Fig. 8c) are (sometimes) captured, the induced barotropic vorticity does not cause barotropic divergence in the free troposphere or moisture convergence in the ABL.

Jiang et al. (2004) have also emphasized the role of moisture–convection feedback induced via two distinct processes. One of them is moisture advection by the mean southerly in the ABL, which is not significant here, as the intraseasonal variability is quite weak in the ABL (see Fig. 4). The other one is moisture advection due to the mean meridional specific humidity gradient, thus implying dry air intrusion from the south just like in our case. Although the mean moisture gradient does exhibit a northward increasing gradient, as shown in Fig. 8b, the major source of asymmetry comes from the asymmetry in the first-baroclinic meridional wind rather than the moisture gradient. In fact, our initial setup is a radiative–convective equilibrium with a uniform moisture background. So the moisture background seen in Fig. 5e is a result of the wave activity and not its cause. As we can see from Fig. 2b, convective events begin to propagate away from the equator as soon as they form at day 0. All the background seems to imply is the inhibition of new convection south of the equator. This is further evidence that the beta-induced asymmetry plays the key role in the northward propagation of BSISO events.

More recent studies by Adames et al. (2016) and Jiang et al. (2018) based on reanalysis data suggested that horizontal advection of the mean moisture by anomalous winds is largely responsible for the northward propagation of the BSISO based on the fact that zonal advection was found to dominate the moisture tendency budget. These observational results are consistent with the work of Biello and Majda (2010), who showed through asymptotic analysis that zonal advection of moisture is an order of magnitude larger that its meridional counterpart in the local Hadley-like setting of tropical dynamics.

Because of the limitation of zonal symmetric assumption, it is impossible to discuss effects of the zonal moisture advection in this model, and thus the moisture-budget results are not consistent with observations because of the lack of zonal dependence. However, it is worth mentioning that the maximum value of moisture anomalies associated with northward-propagating events (about 2 K) in Fig. 6e is much weaker than that of the climatological-mean moisture (about 6.5 K) in Fig. 5e. Surprisingly, the corresponding mean moisture gradient is much weaker than the anomalous moisture gradient, as shown in Figs. 8a and 8b. The essential reason for such a weak mean moisture gradient is due to the local maxima and minima of climatological-mean moisture near the latitude 8° and 13°N, respectively. That said, the results obtained here clearly suggest that while the meridional advection of moisture might be relatively weaker than its horizontal counterpart (in the 3D setting), it plays a primary role in the northward propagation of BSISO, besides the dominant contribution by the zonal moisture advection as concluded in Jiang et al. (2018).

As mentioned in section 6, the sensitivity experiment with the slightly varied SST in SON still features persistent northward propagation, indicating the robustness of the model. However, this result is at odds with the observation that the northward-propagating ISO signals are mainly observed during boreal summer (JJA) but are suppressed during boreal autumn (SON; Lau and Waliser 2011). The essential reason why the model fails to capture the suppressed ISOs during SON may be related to the lack of three-dimensional geometry. Based on a coarse-resolution aquaplanet GCM, Ajayamohan et al. (2014) showed a realistic monsoon ISO with a meridionally tilted monsoon dipole and the meridional seesaw of convection over the Indian sector, followed by northward and then MJO-like eastward propagation over the Southeast Asian sector. In contrast, this model cannot represent the meridionally tilted dipole in zonally symmetric geometry but does capture key features of the northward-propagating ISOs. Presumably, it is the gradually prevailing eastward-propagating MJOs during SON that dominate the intraseasonal variability and result in the suppressed northward-propagating ISOs. Besides, even in the two-dimensional geometry, the seasonal cycle of background moisture stratification may suppress the northward-propagating ISOs during SON, whereas the associated parameters $\tilde{Q}_0$, $\tilde{Q}_1$, $\tilde{Q}_1$ in the model are artificially kept the same in those sensitivity experiments.

We also looked at the mechanisms of initiation near the equator and terminations near 20°N of BSISOs. Our investigation reveals that initiation of new BSISO events is mainly triggered by the second-baroclinic moisture convergence induced by an omnipresent congestus heating background, in the equatorial region, which fades only during and within the active phase of the BSISO events. While this second-baroclinic convergence is overcompensated by the first-baroclinic divergence associated with the preexisting actively propagating BSISO event north of the equator, through the intensification of the local Hadley circulation, it becomes dominant and leads to an intensification of equatorial convection as soon as the preceding BSISO event reaches a high-enough latitude and terminates. This is somewhat consistent with the Hadley cell–wave interaction mechanism suggested by Wang and Xie (1997).

As for the termination, we found that it starts by a weakening of the wave as it approaches the edge of the imposed warm SST profile leading to a weakening of the first-baroclinic meridional velocity and its asymmetry measure, thus nearly stalling the wave and making it vulnerable to precipitation-induced drying and further weakening.

The BSISO events as seen in Fig. 2 are indeed too regular. As an easy way to break this regularity and simulate BSISO events with some intermittency behavior as in nature, one could use the stochastic version of the multicloud parameterization (Khouider et al. 2010; Frenkel et al. 2012), which is based on a birth–death lattice model and has been implemented successfully in general circulation models (e.g., Deng et al. 2015; Goswami et al. 2017b). In fact, De La Chevrotière and Khouider (2017) have already implemented this stochastic parameterization scheme in this zonally symmetric model; however, our first tests with this model were unsuccessful in producing cleanly visible northward-propagating BSISO, although as shown in De La Chevrotière and Khouider (2017) such signals are there, but the noisiness of the simulation made it hard to analyze. With the understanding gained here, we conjecture that the inconclusive results are because strong stochastic fluctuations may have prevented the asymmetry in v_1 to persist at the BSISO scale. This can be easily verified by tuning down the stochastic noise by increasing the number of lattice sites, for example. Moreover, an important future research direction is to test these conclusions in a full 3D setting by either running the same model where the zonal symmetry is relaxed or using cloud-permitting simulations. Last, although the simulated northward-propagating BSISO here is independent of SST variability, a general framework coupling with active SST dynamics may provide new insights on its northward propagation over the Indian Ocean. It should be also interesting to conduct sensitivity experiments with meridionally varying mean moisture stratification coefficients ($\tilde{Q}_0$, $\tilde{Q}_1$, and $\tilde{Q}_2$) and investigate whether the model solution and quantitative aspects of the northward propagation would change.

Acknowledgments. The research of B.K is partially funded by a discovery grant from the Natural Sciences and Engineering Research Council of Canada. This research was done when Q.Y. was visiting the University of Victoria during September–December 2017. The research of A.J.M. is partially supported by the Office of Naval Research ONR MURI N00014-12-1-0912 and the Center for Prototype Climate Modeling (CPCM) in New York University Abu Dhabi (NYUAD) Research Institute. Q. Y. is funded as a postdoctoral fellow by CPCM at the NYUAD Research Institute.

REFERENCES

Adames, Á. F., J. M. Wallace, and J. M. Monteiro, 2016: Seasonality of the structure and propagation characteristics of the MJO. *J. Atmos. Sci.*, **73**, 3511–3526, https://doi.org/10.1175/JAS-D-15-0232.1.

Ajayamohan, R. S., B. Khouider, and A. J. Majda, 2013: Realistic initiation and dynamics of the Madden-Julian Oscillation in a coarse resolution aquaplanet GCM. *Geophys. Res. Lett.*, **40**, 6252–6257, https://doi.org/10.1002/2013GL058187.

——, ——, and ——, 2014: Simulation of monsoon intraseasonal oscillations in a coarse-resolution aquaplanet GCM. *Geophys. Res. Lett.*, **41**, 5662–5669, https://doi.org/10.1002/2014GL060662.

Bellenger, H., K. Yoneyama, M. Katsumata, T. Nishizawa, K. Yasunaga, and R. Shirooka, 2015: Observation of moisture tendencies related to shallow convection. *J. Atmos. Sci.*, **72**, 641–659, https://doi.org/10.1175/JAS-D-14-0042.1.

Biello, J. A., and A. J. Majda, 2005: A multiscale model for the Madden–Julian Oscillation. *J. Atmos. Sci.*, **62**, 1694–1721, https://doi.org/10.1175/JAS3455.1.

——, and ——, 2010: Intraseasonal multi-scale moist dynamics of the tropical atmosphere. *Commun. Math. Sci.*, **8**, 519–540, https://doi.org/10.4310/CMS.2010.v8.n2.a11.

Brunet, G., and Coauthors, 2010: Collaboration of the weather and climate communities to advance subseasonal-to-seasonal prediction. *Bull. Amer. Meteor. Soc.*, **91**, 1397–1406, https://doi.org/10.1175/2010BAMS3013.1.

Chikira, M., 2014: Eastward-propagating intraseasonal oscillation represented by Chikira–Sugiyama cumulus parameterization. Part II: Understanding moisture variation under weak temperature gradient balance. *J. Atmos. Sci.*, **71**, 615–639, https://doi.org/10.1175/JAS-D-13-038.1.

De La Chevrotière, M., and B. Khouider, 2017: A zonally symmetric model for the monsoon-Hadley circulation with stochastic convective forcing. *Theor. Comput. Fluid Dyn.*, **31**, 89–110, https://doi.org/10.1007/s00162-016-0407-8.

Deng, Q., B. Khouider, and A. J. Majda, 2015: The MJO in a coarse-resolution GCM with a stochastic multicloud parameterization. *J. Atmos. Sci.*, **72**, 55–74, https://doi.org/10.1175/JAS-D-14-0120.1.

Drbohlav, H.-K. L., and B. Wang, 2005: Mechanism of the northward-propagating intraseasonal oscillation: Insights from a zonally symmetric model. *J. Climate*, **18**, 952–972, https://doi.org/10.1175/JCLI3306.1.

——, and ——, 2007: Horizontal and vertical structures of the northward-propagating intraseasonal oscillation in the South Asian monsoon region simulated by an intermediate model. *J. Climate*, **20**, 4278–4286, https://doi.org/10.1175/JCLI4244.1.

Emanuel, K. A., 1987: An air–sea interaction model of intraseasonal oscillations in the tropics. *J. Atmos. Sci.*, **44**, 2324–2340, https://doi.org/10.1175/1520-0469(1987)044<2324:AASIMO>2.0.CO;2.

Frenkel, Y., A. J. Majda, and B. Khouider, 2012: Using the stochastic multicloud model to improve tropical convective parameterization: A paradigm example. *J. Atmos. Sci.*, **69**, 1080–1105, https://doi.org/10.1175/JAS-D-11-0148.1.

Fu, X., and B. Wang, 2004: Differences of boreal summer intraseasonal oscillations simulated in an atmosphere–ocean coupled model and an atmosphere-only model. *J. Climate*, **17**, 1263–1271, https://doi.org/10.1175/1520-0442(2004)017<1263:DOBSIO>2.0.CO;2.

Gill, A. E., 1982: *Atmosphere–Ocean Dynamics*. Academic Press, 662 pp.

Goswami, B. B., B. Khouider, R. Phani, P. Mukhopadhyay, and A. J. Majda, 2017a: Improved tropical modes of variability in the NCEP Climate Forecast System (version 2) via a stochastic multicloud model. *J. Atmos. Sci.*, **74**, 3339–3366, https://doi.org/10.1175/JAS-D-17-0113.1.

——, ——, ——, ——, and ——, 2017b: Improving synoptic and intraseasonal variability in CFSv2 via stochastic representation of organized convection. *Geophys. Res. Lett.*, **44**, 1104–1113, https://doi.org/10.1002/2016GL071542.

Hendon, H. H., and B. Liebmann, 1994: Organization of convection within the Madden-Julian Oscillation. *J. Geophys. Res.*, **99**, 8073–8084, https://doi.org/10.1029/94JD00045.

——, and M. L. Salby, 1994: The life cycle of the Madden–Julian Oscillation. *J. Atmos. Sci.*, **51**, 2225–2237, https://doi.org/10.1175/1520-0469(1994)051<2225:TLCOTM>2.0.CO;2.

Hohenegger, C., and B. Stevens, 2013: Preconditioning deep convection with cumulus congestus. *J. Atmos. Sci.*, **70**, 448–464, https://doi.org/10.1175/JAS-D-12-089.1.

Jiang, X., and N.-C. Lau, 2008: Intraseasonal teleconnection between North American and western North Pacific monsoons with 20-day time scale. *J. Climate*, **21**, 2664–2679, https://doi.org/10.1175/2007JCLI2024.1.

——, and D. E. Waliser, 2009: Two dominant subseasonal variability modes of the eastern Pacific ITCZ. *Geophys. Res. Lett.*, **36**, L04704, https://doi.org/10.1029/2008GL036820.

——, T. Li, and B. Wang, 2004: Structures and mechanisms of the northward propagating boreal summer intraseasonal oscillation. *J. Climate*, **17**, 1022–1039, https://doi.org/10.1175/1520-0442(2004)017<1022:SAMOTN>2.0.CO;2.

——, and Coauthors, 2015: Vertical structure and physical processes of the Madden-Julian Oscillation: Exploring key model physics in climate simulations. *J. Geophys. Res.*, **120**, 4718–4748, https://doi.org/10.1002/2014JD022375.

——, Á. F. Adames, M. Zhao, D. Waliser, and E. Maloney, 2018: A unified moisture mode framework for seasonality of the Madden–Julian Oscillation. *J. Climate*, **31**, 4215–4224, https://doi.org/10.1175/JCLI-D-17-0671.1.

Johnson, R. H., T. M. Rickenbach, S. A. Rutledge, P. E. Ciesielski, and W. H. Schubert, 1999: Trimodal characteristics of tropical convection. *J. Climate*, **12**, 2397–2418, https://doi.org/10.1175/1520-0442(1999)012<2397:TCOTC>2.0.CO;2.

Kemball-Cook, S., and B. Wang, 2001: Equatorial waves and air–sea interaction in the boreal summer intraseasonal oscillation. *J. Climate*, **14**, 2923–2942, https://doi.org/10.1175/1520-0442(2001)014<2923:EWAASI>2.0.CO;2.

Khouider, B., 2018: *Models for Tropical Climate Dynamics: Waves, Clouds, and Precipitation.* Springer, 300 pp.

——, and A. J. Majda, 2005: A non-oscillatory well balanced scheme for an idealized tropical climate model. Part I: Algorithm and validation. *Theor. Comput. Fluid Dyn.*, **19**, 331–354, https://doi.org/10.1007/s00162-005-0170-8.

——, and ——, 2006a: Multicloud convective parametrizations with crude vertical structure. *Theor. Comput. Fluid Dyn.*, **20**, 351–375, https://doi.org/10.1007/s00162-006-0013-2.

——, and ——, 2006b: A simple multicloud parameterization for convectively coupled tropical waves. Part I: Linear analysis. *J. Atmos. Sci.*, **63**, 1308–1323, https://doi.org/10.1175/JAS3677.1.

——, and ——, 2008a: Equatorial convectively coupled waves in a simple multicloud model. *J. Atmos. Sci.*, **65**, 3376–3397, https://doi.org/10.1175/2008JAS2752.1.

——, and ——, 2008b: Multicloud model for organized tropical convection: Enhanced congestus heating. *J. Atmos. Sci.*, **65**, 895–914, https://doi.org/10.1175/2007JAS2408.1.

——, J. A. Biello, and A. J. Majda, 2010: A stochastic multicloud model for tropical convection. *Commun. Math. Sci.*, **8**, 187–216, https://doi.org/10.4310/CMS.2010.v8.n1.a10.

——, A. St-Cyr, A. J. Majda, and J. Tribbia, 2011: The MJO and convectively coupled waves in a coarse resolution GCM with a simple multicloud parameterization. *J. Atmos. Sci.*, **68**, 240–264, https://doi.org/10.1175/2010JAS3443.1.

Kiladis, G. N., M. C. Wheeler, P. T. Haertel, K. H. Straub, and P. E. Roundy, 2009: Convectively coupled equatorial waves. *Rev. Geophys.*, **47**, RG2003, https://doi.org/10.1029/2008RG000266; Corrigendum, **49**, RG3004, https://doi.org/10.1029/2011RG000370.

Kim, D., J.-S. Kug, and A. H. Sobel, 2014: Propagating versus nonpropagating Madden–Julian Oscillation events. *J. Climate*, **27**, 111–125, https://doi.org/10.1175/JCLI-D-13-00084.1.

Lau, W. K.-M., and D. E. Waliser, 2011: *Intraseasonal Variability in the Atmosphere–Ocean Climate System.* 2nd ed. Springer, 614 pp.

Lawrence, D. M., and P. J. Webster, 2002: The boreal summer intraseasonal oscillation: Relationship between northward and eastward movement of convection. *J. Atmos. Sci.*, **59**, 1593–1606, https://doi.org/10.1175/1520-0469(2002)059<1593:TBSIOR>2.0.CO;2.

Lee, J.-Y., B. Wang, M. C. Wheeler, X. Fu, D. E. Waliser, and I.-S. Kang, 2013: Real-time multivariate indices for the boreal summer intraseasonal oscillation over the Asian summer monsoon region. *Climate Dyn.*, **40**, 493–509, https://doi.org/10.1007/s00382-012-1544-4.

Madden, R. A., 1986: Seasonal variations of the 40–50 day oscillation in the tropics. *J. Atmos. Sci.*, **43**, 3138–3158, https://doi.org/10.1175/1520-0469(1986)043<3138:SVOTDO>2.0.CO;2.

——, and P. R. Julian, 1971: Detection of a 40–50 day oscillation in the zonal wind in the tropical pacific. *J. Atmos. Sci.*, **28**, 702–708, https://doi.org/10.1175/1520-0469(1971)028<0702:DOADOI>2.0.CO;2.

——, and ——, 1972: Description of global-scale circulation cells in the tropics with a 40–50 day period. *J. Atmos. Sci.*, **29**, 1109–1123, https://doi.org/10.1175/1520-0469(1972)029<1109:DOGSCC>2.0.CO;2.

Majda, A. J., and S. N. Stechmann, 2009: The skeleton of tropical intraseasonal oscillations. *Proc. Natl. Acad. Sci. USA*, **106**, 8417–8422, https://doi.org/10.1073/pnas.0903367106.

——, B. Khouider, and Y. Frenkel, 2015: Effects of rotation and mid-troposphere moisture on organized convection and convectively coupled gravity waves. *Climate Dyn.*, **44**, 937–960, https://doi.org/10.1007/s00382-014-2222-5.

Pauluis, O., 2004: Boundary layer dynamics and cross-equatorial Hadley circulation. *J. Atmos. Sci.*, **61**, 1161–1173, https://doi.org/10.1175/1520-0469(2004)061<1161:BLDACH>2.0.CO;2.

Raymond, D. J., 2001: A new model of the Madden–Julian Oscillation. *J. Atmos. Sci.*, **58**, 2807–2819, https://doi.org/10.1175/1520-0469(2001)058<2807:ANMOTM>2.0.CO;2.

Reynolds, R. W., N. A. Rayner, T. M. Smith, D. C. Stokes, and W. Wang, 2002: An improved in situ and satellite SST analysis for climate. *J. Climate*, **15**, 1609–1625, https://doi.org/10.1175/1520-0442(2002)015<1609:AIISAS>2.0.CO;2.

Romps, D. M., 2014: Rayleigh damping in the free troposphere. *J. Atmos. Sci.*, **71**, 553–565, https://doi.org/10.1175/JAS-D-13-062.1.

Seo, K.-H., J.-K. E. Schemm, W. Wang, and A. Kumar, 2007: The boreal summer intraseasonal oscillation simulated in the NCEP Climate Forecast System: The effect of sea surface temperature. *Mon. Wea. Rev.*, **135**, 1807–1827, https://doi.org/10.1175/MWR3369.1.

Sikka, D. R., and S. Gadgil, 1980: On the maximum cloud zone and the ITCZ over Indian longitudes during the southwest monsoon. *Mon. Wea. Rev.*, **108**, 1840–1853, https://doi.org/10.1175/1520-0493(1980)108<1840:OTMCZA>2.0.CO;2.

Stechmann, S. N., A. J. Majda, and B. Khouider, 2008: Nonlinear dynamics of hydrostatic internal gravity waves. *Theor. Comput. Fluid Dyn.*, **22**, 407–432, https://doi.org/10.1007/s00162-008-0080-7.

Waite, M. L., and B. Khouider, 2009: Boundary layer dynamics in a simple model for convectively coupled gravity waves. *J. Atmos. Sci.*, **66**, 2780–2795, https://doi.org/10.1175/2009JAS2871.1.

Wang, B., and X. Xie, 1997: A model for the boreal summer intraseasonal oscillation. *J. Atmos. Sci.*, **54**, 72–86, https://doi.org/10.1175/1520-0469(1997)054<0072:AMFTBS>2.0.CO;2.

——, and Z. Fan, 1999: Choice of South Asian summer monsoon indices. *Bull. Amer. Meteor. Soc.*, **80**, 629–638, https://doi.org/10.1175/1520-0477(1999)080<0629:COSASM>2.0.CO;2.

Wolding, B. O., and E. D. Maloney, 2015: Objective diagnostics and the Madden–Julian Oscillation. Part II: Application to moist static energy and moisture budgets. *J. Climate*, **28**, 7786–7808, https://doi.org/10.1175/JCLI-D-14-00689.1.

Yasunari, T., 1979: Cloudiness fluctuations associated with the Northern Hemisphere summer monsoon. *J. Meteor. Soc. Japan*, **57**, 227–242.

——, 1980: A quasi-stationary appearance of 30 to 40 day period in the cloudiness fluctuations during the summer monsoon over India. *J. Meteor. Soc. Japan*, **58**, 225–229.

Zhang, C., 2005: Madden–Julian Oscillation. *Rev. Geophys.*, **43**, RG2003, https://doi.org/10.1029/2004RG000158.

——, 2013: Madden–Julian Oscillation: Bridging weather and climate. *Bull. Amer. Meteor. Soc.*, **94**, 1849–1870, https://doi.org/10.1175/BAMS-D-12-00026.1.